

Nomenclature

Roman Symbols

tick Unit of time equal to 500 ns

Acronyms / Abbreviations

art analysis reconstruction framework

ADC Analogue to Digital Converter

APA Anode Plane Assembly

CCD Charge-Couple Device

CDR Conceptual Design Review

CMOS Complementary Metal-Oxide Semiconductor

CPA Cathode Plane Assembly

CP Charge-Parity

CRC Cosmic Ray Counter

CRP Charge Readout Planes

CRY Cosmic-ray Shower Library

DUNE Deep Underground Neutrino Experiment

DVR Digital Video Recorder

ECal Electromagnetic Calorimeter

FD Far Detector

Nomenclature

Fermilab Fermi National Lab

FGT Fine-Grained Tracker

FNAL Fermi National Lab

GENIE Generates Events for Neutrino Interaction Experiments

GUT Grand Unified Theory

HV High Voltage

LAr Liquid Argon

LArSoft Liquid Argon Software

LArTPC Liquid Argon Time Projection Chamber

LAS LEM/Anode Sandwiches

LBNE Long Baseline Neutrino Experiment

LBNF Long Baseline Neutrino Facility

LBNO Long Baseline Neutrino Observatory

LEM Large Electron Multipliers

MIP Minimally Ionising Particle

MPV Most Probable Value

MUSIC MUon Simulation Code

MUSUN MUon Simulations UNderground

ND Near Detector

PCB Printed Circuit Board

PD Photon Detector

PID Particle IDentification

PIP-II Proton Improvement Plan II

PMT Photo Multiplier Tubes

Nomenclature

9

PoCA Point of Closest Approach

ROI Region Of Interest

RPC Resistive Plate Chambers

SiPM Silicon Photo Multiplier

SK Super Kamiokande

SM Standard Model

SSP SiPM Signal Processor

SURF Sanford Underground Research Facility

TPC Time Projection Chamber

Chapter 6

Simulations of the DUNE Far Detector

Work presented in Chapters 3, 4 and 5 concerned the 35 ton prototype, however the following simulations have been performed with respect to the DUNE Far Detector (FD). Simulations in the FD have concentrated on cosmogenic background to neutrino oscillations, discussed in Section 6.1, and the muon background to nucleon decay, discussed in Section 6.3. The simulations shown in Section 6.1 are discussed in [152], and were performed for the Long Baseline Neutrino Experiment (LBNE), which along with the Long Baseline Neutrino Observatory (LBNO), formed the basis for DUNE, and so are included here for completeness. The author contributed by incorporating the *complex* detector geometry, and the accurate surface profile into the simulations, though the main body of work was performed by the author of [152]. The other work presented was performed for the DUNE collaboration, in conjunction with work done by Vitaly Kudryavtsev and Matthew Robinson, both of the University of Sheffield. This work was performed with the aim of producing muon-induced background limits to nucleon decay in the DUNE FD.

6.1 Simulations of the LBNE surface detector

A preliminary design of the LBNE experiment had a 10 kt LAr detector on the surface, with a 3 m rock overburden [153]. Due to the large flux of cosmic rays at such a shallow depth, and the relative scarcity of neutrino events, it is necessary to establish whether the cosmic background can be sufficiently removed to allow neutrino interactions to be discerned. In order to show this, a series of simulations using both a simplified, and a more detailed detector design are performed. The cosmogenic backgrounds due to muons, protons and neutrons, are considered. These simulations, unlike other work presented in this thesis, were performed using a stand-alone version of GEANT4, and not in LArSoft. For a more thorough

6.1 Simulations of the LBNE surface detector

180

¹ review of the simulations, see [152].

²

³ Simulations have been built using GEANT4 versions 9.4 and 9.6. Initial simulations
⁴ were performed using version 9.4, before being rebuilt to use version 9.6. A study showing
⁵ that the background rate did not change with the newer version of GEANT4 was performed,
⁶ in order to verify that the two sets of simulations were consistent. In all simulations the
⁷ physics list “Shielding” was used [154]. Shielding allows particles to undergo Compton
⁸ scattering, inelastic scattering with nuclei and nucleons, and includes all electromagnetic
⁹ (EM) processes for all charged particles.

¹⁰

¹¹ The authors work built on initial simulations which were performed using a simplified
¹² geometry, referred to as the *simple* geometry, which consisted of a single box of LAr
¹³ measuring $30 \times 15 \times 16 \text{ m}^3$. This detector was enclosed in rock measuring $(5 \times 10^3) \times$
¹⁴ $(5 \times 10^3) \times 22 \text{ m}^3$, in the x , y , and z coordinates respectively. The detector was positioned
¹⁵ in the rock so as to have a 3 m overburden of rock. As simulations were not performed in
¹⁶ LArSoft, the co-ordinate system used was defined as follows;

¹⁷ • x - parallel to the beam direction.

¹⁸ • y - perpendicular to the beam direction.

¹⁹ • z - vertical direction.

²⁰ • The co-ordinate system is centred on the middle of the detector volume in x and y , and
²¹ on the surface of the rock which was above the detector in z .

²² The results of these initial simulations, discussed in detail in [152], are not shown here, but
²³ will be summarised in Table 6.2.

²⁴

²⁵ The improvements which the author made to these initial simulations were two fold.
²⁶ Firstly a more detailed geometry, referred to as the *complex* geometry, was included, this
²⁷ had a much more realistic detector design [155]. The *complex* geometry had two identical
²⁸ cryostats, each containing 120 TPC cells measuring $2.52 \times 2.28 \times 7.00 \text{ m}^3$. These cells
²⁹ each contain an active volume of LAr measuring $2.27 \times 2.25 \times 6.30 \text{ m}^3$. The TPC cells
³⁰ are arranged such that are 10, 6 and 2 TPC cells in the x , y and z directions, respectively.
³¹ This gives a total volume of LAr in each cryostat measuring $28.20 \times 13.95 \times 15.0 \text{ m}^3$, with
³² a mass of 5.35 kton. This gives a total fiducial mass of 10.7 kton of active LAr in the two
³³ cryostats. Running vertically between the TPC cells are anode plane assemblies (APAs) and
³⁴ cathode plane assemblies (CPA’s), all of which are embedded within the larger blocks of LAr.

6.1 Simulations of the LBNE surface detector

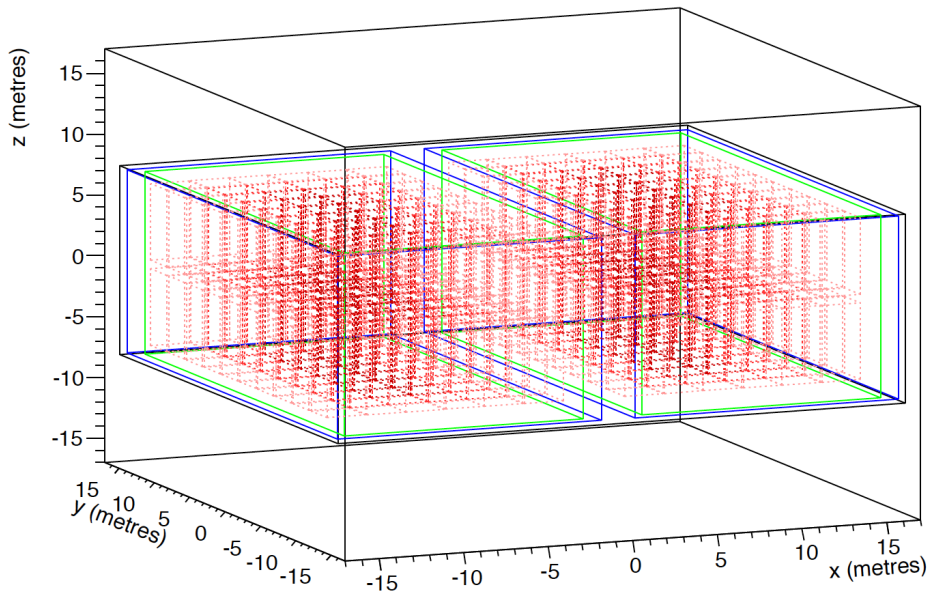


Fig. 6.1 The *complex* detector geometry used in the LBNE surface detector simulations. The TPC cells are shown in red, and are orientated such that there are 10, 6, and 2 TPCs in the x , y , z coordinates of each cryostat respectively. The steel walls of the cryostats are green, whilst the outer edges of polyurethane are blue, and the concrete enclosures are black. Figure taken from [152].

These blocks of LAr are further housed inside stainless steel containers, which are insulated by 0.8 m of polyurethane. The two cryostats are surrounded by 0.5 m of concrete on all sides, with 3 m of concrete separating them. A representation of the detector, produced by the GEANT4 visualisation tool, is shown in Figure 6.1.

Secondly, an accurate surface profile, including the hills surrounding the far detector site was incorporated into the simulations. The proposed location of the LBNE detector was the same as the proposed DUNE detector location, though it was on the surface, and not in the mine. A satellite generated map, centred on SURF, which encompasses an area of 20×20 km² is used to generate the accurate surface profile. The map is sampled in bins measuring 5×5 m². To include the effects that the surrounding hills would have on the muon flux, muons are initially sampled 600 m above the surface, and are then stepped through the surface profile, until they reach a box measuring $80 \times 80 \times 36$ m³ surrounding the detector. The amount of rock that a muon passes through is calculated, and the energy losses which this will cause are then taken into account before subsequent simulations. By taking the surface profile into account in this way, simulation time can be reduced by not having to simulate the surface profile for every new set of muons. The surface profile is modified so as to have a flat

6.1 Simulations of the LBNE surface detector

182

1 surface measuring $100 \times 100 \text{ m}^2$ above the detector location, as it is envisioned that there
2 will be detector out buildings around the detector site. The accurate surface profile is shown
3 in Figure 6.3a, where it is presented in the context of producing muons for the DUNE FD
4 location.

5

6 It should be emphasised that all work presented here has been done using Monte Carlo
7 truth, and so no reconstruction has performed. It also means that at all times only Monte
8 Carlo truth information is used. Therefore, any positions or trajectories which are referred
9 to are those which are recorded by GEANT4 [104]. This information saved by GEANT4 is
10 “smeared” before analysis is performed, in attempt to take into account of some of the detector
11 effects which were not simulated. This smearing is particle type and energy dependant, and
12 is performed on the particles position, trajectory, and energy [152, 156].

13

14 **6.1.1 Classifying signal and background events**

15 Before the simulations can be described in detail, it is necessary to classify what is classified
16 as signal and background event. In the LBNE and DUNE FD, a ν_e appearance signal event
17 would occur when a ν_e undergoes inelastic scattering with either an electron or nucleon. This
18 interaction will produce an electron, which will in turn produce an EM shower. It is this EM
19 shower which will be identified as a neutrino appearance signal. The electron track which is
20 produced in these interactions will not necessarily be isolated, and may be accompanied by
21 hadronic debris.

22

23 However, cosmic ray particles are able to produce signals which mimic this appearance
24 signal. These signal mimicking events can come from a large variety of sources, including,
25 but not limited to, knock-on electrons from muons, bremsstrahlung photons, meson decays
26 to photons, and EM showers which originate outside of the active volume of the detector
27 but then enter it. A background event is then defined as the initial photon in an EM shower.
28 The first generation photon is used as this will contain the total energy of the shower, and
29 removes the need to record every particle produced in the shower. The final position (point
30 of pair production) of the photon is used in all calculations where the position is required,
31 as the photon will not be observed in the actual detector, only the electrons and positrons it
32 produces. Background showers which start with an electron from Compton scattering are not
33 counted, as pair production is the major source of photons at the energies considered here.

34

6.1.2 Description of cuts used

As noted above, the event rate due to cosmic backgrounds will be much larger than the neutrino event rate, and so a series of cuts, designed to remove cosmic background whilst preserving signal events, have to be developed. This section will briefly outline the cuts which were developed to achieve this. A more rigorous definition of the cuts can be found in [152].

The simplest cut considers the energy of the electromagnetic (EM) cascade which is induced. As is the case for DUNE, the LBNE beamline was a broadband neutrino beam, where neutrino analyses would have been concentrated within the 0.25 - 5.0 GeV energy range. This means that any EM cascade which deposited more than 5 GeV of energy, or less than 0.25 GeV of energy into the detector would not be considered as signal events.

As charged particles which enter the detector will produce tracks, it is possible to calculate the minimum separation between these charged tracks and the point at which a photon pair produces. This Point of Closest Approach (PoCA), is calculated by extrapolating the trajectory of the photon backwards from the location at which it pair produces, towards the charged particle tracks. The charged particle tracks are also extrapolated backwards, and so the smallest separations may be outside of the active volume of the detector. A photon is identified as being due to the charged particle track if the PoCA is below a certain threshold. Should a photon be due to a charged particle track, then it is identified as being a background event. Thresholds of 30 cm and 10 cm are used when considering the initial charged muon, and all charged particles respectively. The latter threshold is smaller to avoid removing signal events, and also has a lower limit of 2 cm, meaning that any photons which have PoCAs of less than 2 cm are not identified as background events. This is because it is possible that charged hadrons are produced at the neutrino interaction vertex, and so the electron produced would have a charged particle very close to it, meaning that were this lower limit not in place, it would fail the all charged PoCA cut.

It has been found that the angle of a neutrino event, with respect to the neutrino beam, is highly correlated to the energy of the neutrino [157]. This means that it is possible to use the angle of a shower with respect to the beam, to distinguish between signal and backgrounds events. The effectiveness of this constraint is highly energy dependant, as any high energy photons which are not tightly correlated to the beam axis will be identified as backgrounds, though few low energy photons will be [158]. An example of how the PoCA, and angle of a

6.1 Simulations of the LBNE surface detector

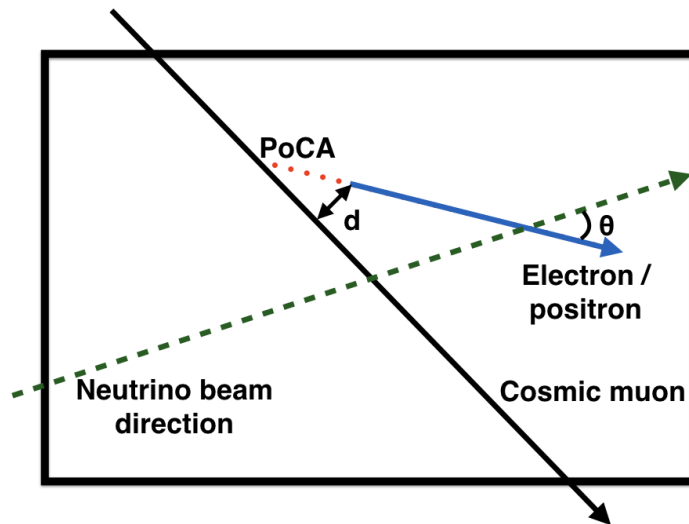


Fig. 6.2 A diagram of the PoCA, and the angle w.r.t the beam calculations in the LBNE surface detector simulations. A cosmic muon which passes through the detector is shown as a black line, whilst an electron/positron that is produced is shown as a blue line. The minimum distance between the muon and electron/positron is shown (d), as well as the point of closest approach (PoCA) when the electron/positron track is extrapolated backwards. The extrapolated track is shown as a dotted red line. The neutrino beam direction is shown as a dashed green line, and the angle that the electron/positron makes with respect to this is shown (θ). Figure is modified from [152].

¹ photon with respect to the beam axis are calculated is shown in Figure 6.2.

²

³ It is envisioned that not all of the instrumented LAr will be able to used to identify
⁴ neutrino events. This is because a fiducial cut will be applied around the detector edges, in
⁵ order to ensure that the entire track is contained within the active volume of the detector.
⁶ For the *complex* detector, this fiducial cut is only applied to the outward facing edges of the
⁷ active volumes. This is because it is assumed that tracks passing between cells, within a
⁸ given cryostat, will be able to be stitched together, as is done in LArSoft.

⁹

¹⁰ Additionally, signal events should be able to be distinguished from background events
¹¹ based on the energy deposition measurements. These will come from identifying the start of
¹² an EM shower as coming from either an electron, or a photon, in the case of a signal, and
¹³ background event, respectively. Studies have shown that the failure rate of this separation
¹⁴ tails off at 10% for showers with energies above 0.5 GeV [159]. Therefore, a flat reduction
¹⁵ of 1/10 is applied to all surviving simulated background events.

¹⁶

Finally, it is envisioned that an efficient photon detection system will be used, which uses the scintillation light emitted by excited argon [160]. This efficient photon detection system should be able to provide information on individual events, and so identify whether a candidate event occurred within the beam spill. If this is used, then the effective drift time of the detector can be reduced from 1400 μs to only 10 μs , a reduction by a factor of 140. This is also applied as a flat reduction to all surviving background events.

6.1.3 Generating particles for background studies

When simulating the cosmogenic background for a detector on the surface it is necessary to simulate the backgrounds due to muons, protons, neutrons and photons. It was found that the background due to cosmic photons was negligible [152], and so they are not discussed here.

The muons used in the simulations are generated using a Gaisser's parameterisation [161], which has been modified for large zenith angles, and muon decay [162]. The differential muon intensity at sea level ($\frac{dI_\mu}{dE_\mu d\Omega}(E_\mu, \theta)$), in units of $\text{cm}^{-2}\cdot\text{s}^{-1}\cdot\text{sr}^{-1}\cdot\text{GeV}^{-1}$, is shown in Equation 6.1.

$$\begin{aligned} \frac{dI_\mu}{dE_\mu d\Omega}(E_\mu, \theta) = & A \times 0.14 \times (E_\mu + \Delta)^{-\gamma} \times p_d \\ & \times \left[\frac{1}{1 + \frac{1.1(E_\mu + \Delta)\cos\theta^*}{115\text{GeV}}} + \frac{0.054}{1 + \frac{1.1(E_\mu + \Delta)\cos\theta^*}{850\text{GeV}}} + R_c \right] \end{aligned} \quad (6.1)$$

where E_μ is the muon energy in GeV at the surface, θ is zenith angle at the height of muon production, $\cos\theta^* = \sqrt{1 - 0.99(1 - \cos^2\theta)}$, Δ is the muon energy loss in the atmosphere and is equal to $\frac{1030 \times 2.06 \times 10^{-3}}{\cos\theta - 120}$, R_c is the ratio of prompt muons to pions, and p_d is the probability for a muon to not decay in the atmosphere [163]. There is also a normalisation constant A , and a spectral index γ , which can both be chosen to fit experimental data. When considering shallow depths, or surface locations, values of $A = 0.1$ and $\gamma = 2.7$ are used [161]. When considering larger depths, as will be done in Sections 6.2 and 6.3 where MUSUN [110, 111] is used, typical values are $A = 1.84$ and $\gamma = 2.77$.

The protons and neutrons used in the simulations are generated using CRY [107, 108], on a plane measuring $50 \times 50 \text{ m}^2$ in the xy plane. It is not necessary to generate protons and neutrons over a large area as their interaction lengths are much shorter than muons, and so protons and neutrons at large angles which pass through large amounts of rock will not be a se-

6.1 Simulations of the LBNE surface detector

186

Table 6.1 The minimum energies of simulated particles, when determining the cosmogenic background for the LBNE surface detector. The percentage of background events which are caused by particles of these energies, or above, is shown. The percentage of the particle flux above this energy, is also shown. It can be seen that, with appropriate minimum energy constraints, it is possible to avoid simulating over 80% of the muon flux, 99% of the proton flux, and 95% of the neutron flux. Table taken from [152].

Primary particle	Min. energy simulated (GeV)	Background (%)	Particle flux (%)
Muons	10	92.3	19.6
Proton	10	92.7	0.76
Neutrons	1	95.6	6.5

1 rious concern. The particles are generated at an altitude of 2100 m above sea level. However,
 2 the LBNE surface detector would have had an altitude of 1505 m above sea level, and so the
 3 particle fluxes generated by CRY have to be corrected to the particle fluxes expected at 1505
 4 m above sea level [152]. The fluxes generated by CRY are also subject to a further correction,
 5 as CRY underestimates the cosmic ray flux by as much as 70% [164]. This is because CRY
 6 only considers protons striking the Earth's atmosphere. As the muon flux is calculated at
 7 sea level, this flux also has to be corrected so as to be the flux at 1505 m above sea level [152].
 8

9 To reduce simulation time, only particles which will cause background events are simu-
 10 lated. For example, it is found that 92.7% of the proton induced background events are due
 11 to protons with energies of 10 GeV or more, yet these particles represent only 0.76% of the
 12 total proton flux. This means that by not simulating protons with energies below 10 GeV, the
 13 vast majority of background events will be simulated, but this will require less than 1% of
 14 the simulation time. The background events which are not simulated, can be accounted for
 15 by correcting the background seen from simulations, by the proportion of background events
 16 which were not simulated [152]. The minimum energies of the simulated muons, protons,
 17 and neutrons, along with the percentage of background events which they cause, and the
 18 percentage of the particle fluxes above this energy, are shown in Table 6.1.

19
 20 From Table 6.1 it can be seen that in the case of only simulating protons above 10 GeV,
 21 7.3% of the background were not simulated, and so the background rate from simulations
 22 should be scaled by a factor of 1.0787 ($\frac{1}{0.927}$).
 23

Table 6.2 The normalised annual background rate for the *simple* detector geometry, separated by particle species, using the flat surface profile. The rates for muons entering the detector, muons missing the detector, proton induced events, and neutron induced events are shown. The annual background for muons entering the detector is only an approximate value, as initial simulations were performed without saving proton hit information, the inclusion of which greatly increases the accuracy of the all charge PoCA cut. Table is taken from [152].

Primary particle	Annual background rate
Muons entering	≈ 1.18
Muons missing	0.11 ± 0.02
Protons	2.57 ± 0.08
Neutrons	1.23 ± 0.07
Total	≈ 5

6.1.4 Results from background simulations

Before the results of the simulations involving the *complex* geometry, and accurate surface profile are discussed, it is useful to briefly summarise the results of the simulations using the *simple* geometry, and flat surface profile. This is shown in Table 6.2.

It can be seen from Table 6.2 that the overall background rate is dominated by hadronic components of the cosmic flux. It is expected that the additional shielding in the *complex* geometry will suppress these components significantly. The annual background induced by cosmic muons has been split into events where the muon enters the detector, and events where it does not enter the detector. This is because when a muon does not enter the detector, the PoCA with respect to the initial muon cannot be calculated. It will also be instructive to observe how the background from each case changes, as the detector geometry is made more accurate. The *complex* geometry, has both a larger surface area and a larger active volume of LAr, therefore it is expected that the muon fluxes will increase. This increase may be quite large for muons which miss the active volume of the detector, as muons may pass through the vertical gaps between TPC volumes and produce secondaries which enter the active volume of the detector. Events like this would, at first glance at least, appear very similar to a neutrino event, as they will be isolated in the centre of the detector.

Only results for the *complex* geometry and accurate surface profile are shown. A separate set of simulations where the annual background when using the *complex* geometry and simple surface profile are shown in [152]. However, as discussed in [152], these background rates were found to be consistent with the background rates for the *complex* geometry and accurate

6.1 Simulations of the LBNE surface detector

Table 6.3 The normalised annual background rate, for events where a primary muon enters the active volume of the detector, for the *complex* geometry and accurate surface profile. A total of 2×10^8 muons with energies greater than 10 GeV are generated, representing 0.1003 years worth of detector live time. The background rate is separated into different first generation photon ancestries. The application of the cuts outlined in Section 6.1.2 is shown, where E_γ is the 0.25 - 5.0 GeV cut, $PoCA_\mu$ is the PoCA w.r.t. the initial muon cut, $\theta_{beam}(E)$ is the energy dependant cut on the angle between the beam and photon trajectory, $PoCA_{all}$ is the PoCA w.r.t. all charged particles cut, $D > 30$ is the 30 cm fiducial cut. Following this, two scaling factors of 1/10 and 1/140, representing the e- γ separation, and the use of an efficient photon detection system respectively, are applied. The errors quoted are Gaussian, unless the simulated annual background rate drops to 0, in which case an upper limit at 90% confidence level [165] is used, with any scaling factors being applied to this limit. No errors are quoted if the error is less than 1% of the simulated annual background rate. Table is taken from [152].

	E_γ	$PoCA_\mu$	$\theta_{beam}(E)$	$PoCA_{all}$	$D > 30$ cm	$e - \gamma(E)$	γ detection
<i>Total</i>	1.32×10^7	$(6.38 \pm 0.09) \times 10^4$	$(2.87 \pm 0.06) \times 10^4$	3796 ± 229	2854 ± 199	285 ± 20	2.03 ± 0.14
$\pi^0 \rightarrow \gamma$	2.24×10^6	$(5.82 \pm 0.09) \times 10^4$	$(2.62 \pm 0.06) \times 10^4$	3339 ± 215	2743 ± 195	274 ± 20	1.96 ± 0.14
$Ext \rightarrow \gamma$	4.48×10^6	5237 ± 270	2425 ± 183	457 ± 80	111 ± 39	11.1 ± 3.9	0.08 ± 0.03
$\mu \rightarrow \gamma$	6.36×10^6	0 – 34	0 – 15.20	0 – 2.01	0 – 1.51	0 – 0.15	0 – 0.001
$Other \rightarrow \gamma$	7.87×10^4	333 ± 68	97 ± 37	0 – 15.20	0 – 11.43	0 – 0.11	0 – 0.002

1 surface profile.

2

3 Table 6.3 shows the background rate for muons which enter the active volume of detector,
4 as sequential cuts are applied, for the *complex* geometry, and accurate surface profile. A total
5 of 2×10^8 muons with energies greater than 10 GeV are generated, representing 0.1003
6 years worth of detector live time. The overall number of background mimicking events is
7 seen to increase when using the *complex* detector geometry, and the accurate surface profile,
8 as opposed to using the *simple* detector geometry, and simple surface profile. It is observed
9 that the expected annual background rates for the *complex* detector geometry in the flat,
10 and accurate surface profiles, are consistent. This means that including the accurate surface
11 profile does not have a significant effect on the background rate.

12

13 The effectiveness of the PoCA cut with respect to the initial muon is obvious, as the
14 annual background event rate is reduced by over 99%. The rejection rate is observed to be
15 100% when considering the $\mu \rightarrow \gamma$ photon ancestry. The rejection rate is also very high in
16 the $Ext \rightarrow \gamma$ photon ancestry where it approaches 100%, this is because when the photons
17 trajectories are extrapolated backwards, they are seen to be very close to the muon track
18 outside the detector. The remaining background is dominated by photons with π^0 parents.
19 Around half of the surviving events are removed by the application of the angular cut, but

6.1 Simulations of the LBNE surface detector

189

Table 6.4 The normalised annual background rate, for events where a primary muon misses the active volume of the detector, for the *complex* geometry and accurate surface profile. A total of 2×10^8 muons with energies greater than 10 GeV are generated, representing 0.1003 years worth of detector live time. The background rate is separated into different first generation photon ancestries. The application of the cuts outlined in Section 6.1.2 is shown. Table is taken from [152].

	E_γ	$D > 30$ cm	$\theta_{beam}(E)$	PoCA _{all}	$e - \gamma(E)$	γ detection
<i>Total</i>	19800 ± 500	4004 ± 235	1551 ± 147	914 ± 113	91 ± 11	0.65 ± 0.08
$\pi^0 \rightarrow \gamma$	3284 ± 213	1108 ± 123	526 ± 85	166 ± 48	16.63 ± 4.80	0.12 ± 0.03
$Ext \rightarrow \gamma$	16500 ± 500	2858 ± 199	998 ± 118	748 ± 102	75 ± 10	0.53 ± 0.07
$Other \rightarrow \gamma$	28 ± 5	28 ± 5	28 ± 5	$0 - 20$	$0 - 2.01$	$0 - 0.01$

more than 80% of these events are removed by the application of the all charged PoCA cut. This again shows how powerful the use of the PoCA cut is when rejecting background events. Whilst the fiducial cut is seen to be effective at removing the remaining $Ext \rightarrow \gamma$ events, this is not the case for the $\pi^0 \rightarrow \gamma$ events. Therefore, the development of efficient methods of e- γ separation, and the use of an efficient photon detection system are critical in reducing the annual background to a rate which would not be prohibitive to observing neutrino interactions.

The background rate for the *complex* detector geometry, and accurate surface profile, for muons which miss the active volume of the detector, is shown in Table 6.4. The same muons used in Table 6.3 are used here, meaning that a detector live time of 0.1003 years has been simulated. The overall number of background mimicking events is seen to increase substantially when using the *complex* detector geometry, and the accurate surface profile, as opposed to using the *simple* detector geometry, and simple surface profile. This is to be expected, as there is a much larger external surface area, and the vertical gaps produce internal gaps between the TPCs. It is observed that the expected annual background rates for the *complex* detector geometry in the flat, and accurate surface profiles, are consistent, though the total number of background events is less when the accurate surface profile is used.

Table 6.4 shows that muons which miss the active volume of the detector cause much fewer background events than those which strike the active volume of the detector. However, the events which they do cause, are much more likely to survive the application of all cuts. This is due to a combination of both the fiducial cut being less effective, and there being more external photons. Both of these differences are caused by muons which pass through gaps between TPCs, and produce secondaries which are far away from the detector walls. These events will produce photons which are not removed by the fiducial cut, and are identified as external photons, as the muon in these events did not produce a track.

6.1 Simulations of the LBNE surface detector

190

Table 6.5 The normalised annual background rate, for proton induced events, for the *complex* geometry. A total of 1×10^7 protons with energies greater than 10 GeV are generated, representing 2.482 years worth of detector live time. The background rate is separated into different first generation photon ancestries. The application of the cuts outlined in Section 6.1.2 is shown. Table is taken from [152].

	E_γ	$D > 30$ cm	$\theta_{beam}(E)$	PoCA _{all}	$e - \gamma(E)$	γ detection
<i>Total</i>	1.55×10^4	$10559 \pm$	3475 ± 39	319 ± 12	31.9 ± 1.2	0.23 ± 0.01
$\pi^0 \rightarrow \gamma$	1.18×10^4	9277 ± 63	3098 ± 36	297 ± 11	29.7 ± 1.1	0.21 ± 0.01
$Ext \rightarrow \gamma$	3120 ± 37	858 ± 19	279 ± 11	22 ± 3	2.2 ± 0.3	0.016 ± 0.002
<i>Other</i> $\rightarrow \gamma$	524 ± 15	424 ± 15	97 ± 6	$0 - 1.04$	$0 - 0.10$	$0 - 0.001$

¹ There will also be more external photons, as the surface area of the detector has substantially increased now that there are two identical cryostats, as opposed to a single block of LAr.

³

⁴ Table 6.5 shows the background rate for protons, as sequential cuts are applied, for the ⁵ *complex* geometry, and accurate surface profile. A total of 1×10^7 protons with energies ⁶ greater than 10 GeV are generated, representing 2.482 years worth of detector live time.

⁷ As the protons are generated on a plane which measures 50×50 m², and the accurate ⁸ surface profile was modified to have a flat area above the detector measuring 100×100 m², ⁹ it is not necessary to propagate protons through the accurate surface profile. As discussed ¹⁰ earlier, protons are generated on a plane measuring 50×50 m² as protons will not induce ¹¹ background events at the high inclinations which muons do. The overall number of back- ¹² ground mimicking events is seen to decrease substantially when using the *complex* detector ¹³ geometry, as opposed to using the *simple* detector geometry.

¹⁴

¹⁵ It can be seen from Table 6.5 that the cut with respect to the beam angle, and the PoCA ¹⁶ calculation with respect to all charged particles, are very effective as they remove 67% and ¹⁷ 90% of all remaining background events respectively. That the all charged PoCA cut is so ¹⁸ effective is not surprising, as many of the photons produced will be close to the initial proton ¹⁹ that was simulated. After all cuts are applied, the annual number of background events is ²⁰ seen to decrease by over a factor of 10 when using the *complex* geometry. This decrease is ²¹ attributed to the additional shielding which is present in the *complex* geometry, as concrete, ²² insulation and inactive regions of LAr have been added.

²³

²⁴ Table 6.6 shows the background rate for neutrons, as sequential cuts are applied, for the ²⁵ *complex* geometry, and accurate surface profile. A total of 1.1×10^8 neutrons with energies ²⁶ greater than 1 GeV are generated, representing 0.653 years worth of detector live time. The ²⁷ neutrons are generated on a plane which measures 50×50 m², and so as seen with the

Table 6.6 The normalised annual background rate, for neutron induced events, for the *complex* geometry. A total of 1.1×10^8 neutrons with energies greater than 1 GeV are generated, representing 0.653 years worth of detector live time. The background rate is separated into different first generation photon ancestries. The application of the cuts outlined in Section 6.1.2 is shown. Table is taken from [152].

	E_γ	$D > 30$ cm	$\theta_{beam}(E)$	PoCA _{all}	$e - \gamma(E)$	γ detection
<i>Total</i>	8405 ± 113	5697 ± 93	1949 ± 54	225 ± 18	22.5 ± 1.8	0.16 ± 0.01
$\pi^0 \rightarrow \gamma$	6397 ± 98	5050 ± 87	1744 ± 51	194 ± 17	19.4 ± 1.7	0.14 ± 0.01
$Ext \rightarrow \gamma$	1796 ± 52	470 ± 26	169 ± 16	30.1 ± 6.7	3.01 ± 0.67	0.021 ± 0.005
<i>Other</i> $\rightarrow \gamma$	209 ± 18	175 ± 16	36.2 ± 7.4	$0 - 3.68$	$0 - 0.37$	$0 - 0.003$

protons, it is unnecessary to propagate neutrons through the accurate surface profile. The overall number of background mimicking events is seen to decrease substantially when using the *complex* detector geometry, as opposed to using the *simple* detector geometry.

From Table 6.6 it can be seen that as was the case with the protons, the cut with respect to the beam angle, and the PoCA calculation with respect to all charged particles, are very effective. Upon the application of all cuts, the annual expected background from neutrons in the *complex* geometry is seen to decrease by almost an order of magnitude. Whilst this is not as dramatic as the reduction seen when considering proton induced backgrounds, it still represents a significant reduction in the background rate. This reduction is again attributed to the extra shielding which is present in the *complex* geometry.

6.1.5 Summary of simulations for the LBNE surface detector

Taking the sum of the expected background rates from Tables 6.3, 6.4, 6.5 and 6.6 gives an expected cosmogenic background after cuts for the *complex* detector geometry, and accurate surface profile, of 3.07 ± 0.25 events per year. This compares with an expected background rate of ≈ 5 events per year, for the *simple* detector geometry, and flat surface profile. The reduction in background rate is due to the additional shielding present in the *complex* geometry which reduces the hadronic background component from 3.80 ± 0.11 to 0.39 ± 0.01 , a decrease of roughly an order of magnitude. However, the increase in surface area of the detector is found to cause the number of background events caused by muons which both enter and miss the active volume of the detector to increase. This increase is very substantial when considering muons which miss the active volume of the detector. This is summarised in Table 6.7.

Table 6.7 The normalised annual background rate for the *simple* and *complex* detector geometries, separated by particle species, using the flat and accurate surface profiles respectively. The rates for muons entering the detector, muons missing the detector, proton induced events, and neutron induced events are shown. The annual background for muons entering the detector when using the *simple* detector geometry and flat surface profile is only an approximate value, as initial simulations were performed without saving proton hit information. The inclusion of proton hits greatly increases the accuracy of the all charge PoCA cut, however this was only seen in a small sample. Table is taken from [152].

Primary particle	<i>simp.</i> geom. & flat surf. prof.	<i>comp.</i> geom. & acc. surf. prof.
Muons entering	≈ 1.18	2.03 ± 0.24
Muons missing	0.11 ± 0.02	0.65 ± 0.08
Protons	2.57 ± 0.08	0.23 ± 0.01
Neutrons	1.23 ± 0.07	0.16 ± 0.01
Total	≈ 5	3.07 ± 0.25

¹ Following the simulation of large samples of muons, protons, and neutrons, the expected
² background for the LBNE surface detector is found when considering a *complex* detector
³ geometry, and an accurate surface profile. This is compared to the expected background rate
⁴ when using a *simple* detector geometry and flat surface profile [152]. It is observed that the
⁵ effect of the *complex* detector geometry is to reduce the overall background rate, primarily
⁶ due to the additional shielding which it provides. This additional shielding causes the proton
⁷ and neutron induced backgrounds to decrease substantially, as was shown in Table 6.7. It
⁸ is however found that there will be a significant source of backgrounds from muons which
⁹ do not enter the active volume of the detector. This is due to the presence of vertical gaps
¹⁰ between the TPC cells. The effect of incorporating the accurate surface profile is found
¹¹ to be negligible, as the hills only offer minimal amounts of shielding. These simulations
¹² provide a relatively accurate estimate of the expected background for the LBNE surface
¹³ design, although it must be stressed that these studies have been performed using Monte
¹⁴ Carlo truth information, and so have not used reconstruction.

¹⁵

¹⁶ 6.2 The use of MUSUN in LArSoft

¹⁷ The primary muons in the following discussions are all generated using MUSIC [110, 112,
¹⁸ 113] and MUSUN [110, 111], and so a brief overview of them is required. MUSIC first
¹⁹ propagates muons through a medium, defined by the user, for given initial energies. A range
²⁰ of energies between 10^2 GeV and 10^7 GeV are considered, and their energy distributions are

Table 6.8 Muon flux parameters as calculated with MUSIC/MUSUN.

Total flux ($\text{cm}^{-2}\cdot\text{s}^{-1}$)	Mean E_μ (GeV)	Mean slant depth (m w.e)	Mean θ ($^\circ$)
5.66×10^{-9}	283	4532	26

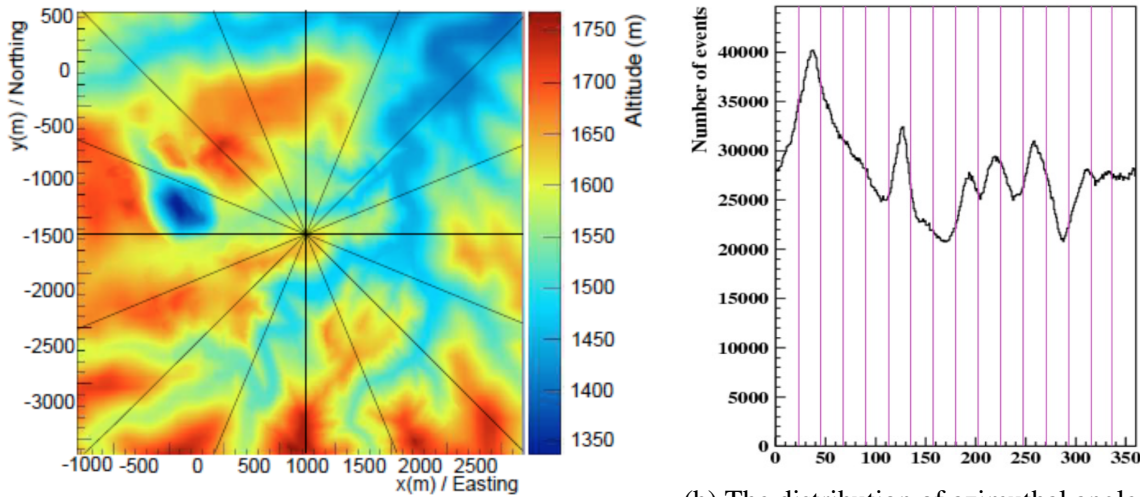
stored at depths of 100 to 15,000 m w.e. Energy losses due to four processes are considered; ionisation, bremsstrahlung, electron-positron pair production and muon-nucleus inelastic scattering. The output of MUSIC, along with the surface muon spectrum parameterisation and the surface profile, is then used by MUSUN to generate a muon energy spectrum and angular distribution, for a given detector location.

The location of the DUNE far detector, near the Ross shaft at SURF, has global coordinates of $44^\circ 20' 45.21''$ North, $103^\circ 45' 16.13''$ West. The rock composition is assumed to be, $\langle Z \rangle = 12.09$ and $\langle A \rangle = 24.17$. The density is assumed to be $2.70 \text{ g}\cdot\text{cm}^{-3}$ [166], though some measurements suggest that it may closer to $2.90 \text{ g}\cdot\text{cm}^{-3}$ [167, 168]. The vertical flux calculated by MUSIC/MUSUN of $5.18 \times 10^{-9} \text{ cm}^{-2}\cdot\text{s}^{-1}\cdot\text{sr}^{-1}$, is well matched to the flux measured by the active veto system of the Davis' experiment, which was $(5.38 \pm 0.07) \times 10^{-9} \text{ cm}^{-2}\cdot\text{s}^{-1}\cdot\text{sr}^{-1}$ [169]. Given the small differences in these values, and another measurement by the Majorana demonstrator [170], the systematic uncertainty in calculating the muon flux is estimated to be 20% [171].

The surface profile around the proposed detector location is shown in Figure 6.3a, where the proposed location is in the centre of the map. Each quadrant on the map has been divided into 4 angles of 22° to help guide the eye when comparing it to Figure 6.3b, where the distribution of azimuth angles is plotted. The vertical lines in Figure 6.3b show the division of the quadrants when the angle is calculated from East to the North. When moving from East to North it is possible to discern how the peaks and troughs on the surface profile, correspond to troughs and peaks, in the distribution of azimuthal angle.

Given these parameters, the muon flux at the DUNE far detector location, when assuming a spherical detector geometry, and without simulating a detector cavern, is given in Table 6.8.

The muons simulated for DUNE are sampled on the surface of a box surrounding the detector hall, which also encompasses 7 m of rock above the cavern, and 5 m of rock on all other sides. This is to ensure that the simulated muons pass through a sufficient amount of rock to induce cascades, both above and around the detector hall. The secondaries produced



(a) The surface profile of the DUNE far detector site at SURF [172].

(b) The distribution of azimuthal angles of muons at the DUNE far detector site at SURF.

Fig. 6.3 The correlation between the surface profile, and the distribution of azimuthal angles at the DUNE far detector site. The quadrants have been divided into four angles of equal size. The azimuthal angle, calculated as the angle from East (pointing to the right in Fig. 6.3a), and increasing counterclockwise, is seen to follow the contours of the surface profile.

1 in these cascades which enter the detector, in the absence of the initial muon, are of particular
 2 interest, as some of them could be mistaken for nucleon decay events. The study of these
 3 nucleon decay mimicking events is discussed in Section 6.3. The size of the box which the
 4 muons are sampled from is $74.43 \times 29.54 \times 30.18 \text{ m}^3$, compared to the simulated cryostat
 5 which has dimensions, $61.62 \times 14.94 \times 13.58 \text{ m}^3$. The dimensions are given as length
 6 \times width \times height, using the LArSoft coordinate system which was defined at the start of
 7 Section 2.6. The muons are sampled according to their energy spectrum, for a given zenith
 8 and azimuthal angle, using the angular distribution obtained with MUSUN.
 9

10 However, before this could be done MUSUN had to be incorporated into the DUNE
 11 software framework, as it had previously been maintained in FORTRAN as an external
 12 package. Before simulations in LArSoft were performed, it was ensured that the muon
 13 distributions produced by the ported LArSoft code were identical to the original distribu-
 14 tions produced by the FORTRAN code. The distributions produced by the DUNE software
 15 framework are shown in Figure 6.4, and are consistent with the distributions made for the
 16 LBNE collaboration [173]. Figure 6.4 shows the initial positions of 10,000 muons around the
 17 simulated DUNE 10 kt module, as generated by LArSoft. The initial positions of the muons

are shown as blue points, whilst the cryostat is a single black box, and each TPC is a red box.

It is found that the muon rate through the box upon which the muons are sampled is 0.1579 Hz. This rate is later used to normalise the background event rate in Section 6.3. Roughly a third of the muons which are generated, pass through the active volume, to give a muon rate through the active volume of 0.053 Hz.

The simulated far detector is contained in an excavated detector hall surrounded by rock. The cryostat is made of concrete, supported by a stainless steel structure. The inside of the cryostat is filled with LAr, which has a total mass of 17.1 kt. Contained within the cryostat is an active volume of LAr measuring $14.5 \times 12 \times 58$ m³, made up of 200 TPCs, to give a total mass of active LAr of 14.1 kt. This figure includes gaps between TPCs, when these are removed, the active mass becomes 13.9 kt of LAr. In Section 6.3 a fiducial cut of 2 cm is used, this causes the fiducial mass to be reduced to 13.8 kt.

6.3 Nucleon decay channels in DUNE

When searching for rare processes, where an experiment is unlikely to see more than a few signal events, an exhaustive study of the potential backgrounds is required. This is so that if a signal is observed, it could provide overwhelming evidence for the process. The search for nucleon decay in DUNE is one such process, and so an extensive study of the background to nucleon decay is required. As discussed in Section 1.2.1, cosmogenic muons cause backgrounds to nucleon decay events, as some of the secondary particles produced by their interactions are able to mimic the nucleon decay signatures. For this reason it is necessary to simulate this background, and to develop a series of cuts which can be applied to the energy depositions which they produce, to establish that they are not due to nucleon decays. When doing this, it is important to use a simulated cosmogenic flux that is as accurate as possible to the one which will be observed by the DUNE far detector. For this reason MUSUN was incorporated into LArSoft, as the muons that it generates correspond to the realistic surface profile, as described in Section 6.2.

The DUNE experiment will run for more than 20 years, and the required statistics for background studies should be even higher than this, so as to ensure the significance of the results. Therefore, a sample of 2×10^9 muons has been generated. Given that the muon flux through the simulated box is 0.1579 Hz, this sample corresponds to 401.6 years of detector

6.3 Nucleon decay channels in DUNE

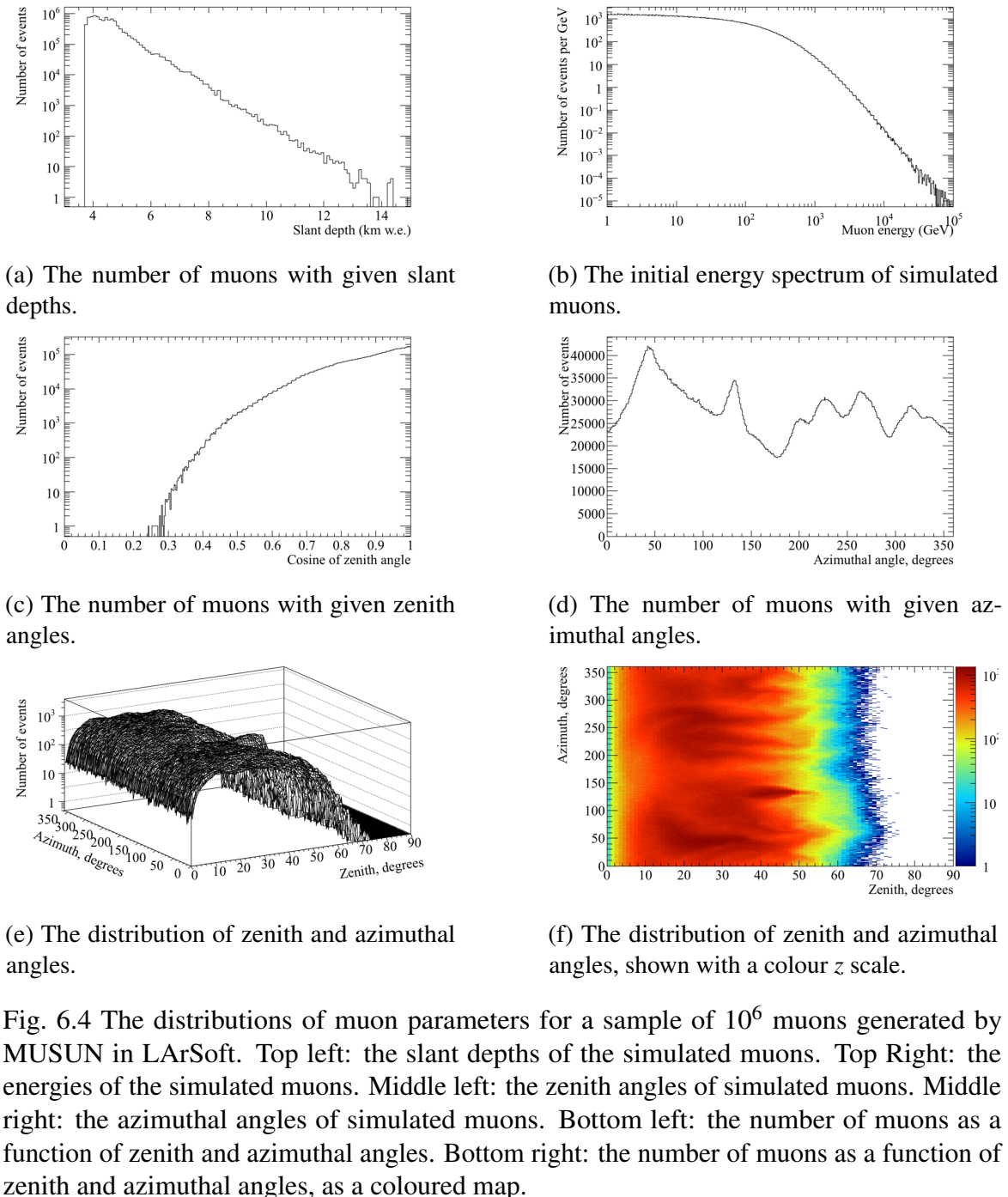


Fig. 6.4 The distributions of muon parameters for a sample of 10^6 muons generated by MUSUN in LArSoft. Top left: the slant depths of the simulated muons. Top Right: the energies of the simulated muons. Middle left: the zenith angles of simulated muons. Middle right: the azimuthal angles of simulated muons. Bottom left: the number of muons as a function of zenith and azimuthal angles. Bottom right: the number of muons as a coloured map.

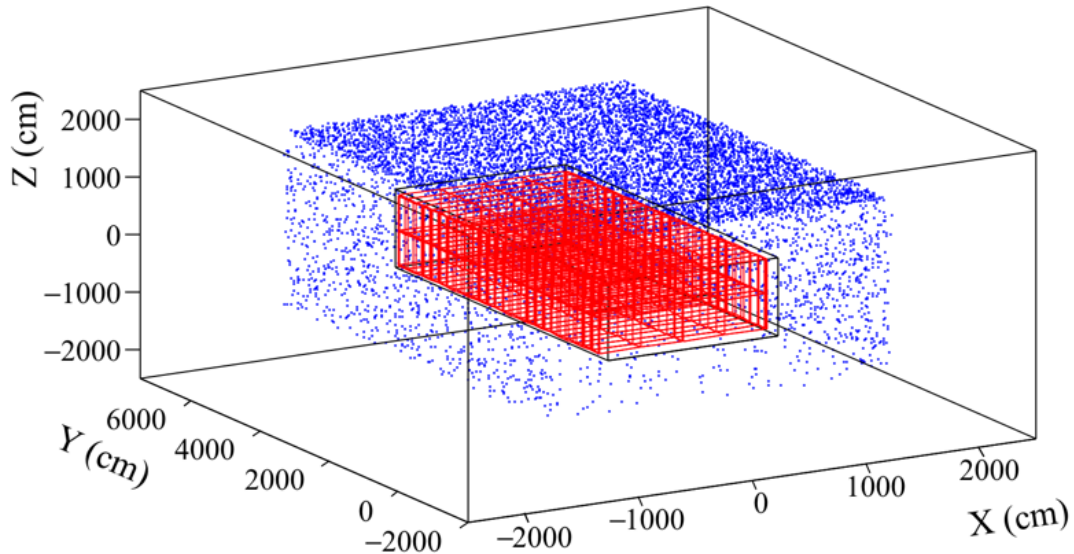


Fig. 6.5 The initial positions of muons generated by MUSUN around a DUNE 10 kt module. The initial positions of the muons are shown as blue points, whilst the cryostat is a single black box and each TPC is a single red box.

live time for a single DUNE FD module. This sample is thus equivalent to 100.4 years of detector live time for the full DUNE design consisting of four FD modules.

Producing samples of this size requires significant computer power, both in terms of running time, and storage space. As a result of this, many of the simulated events are discarded before being saved to disk. This is done through the application of a filter after GEANT4 [104], where events satisfying one of the following cuts are discarded;

- Contain a muon track of more than 1 m.
- There are no energy depositions in the entire detector volume.

This way, events which could mimic nucleon decay signals are not removed from the analyses performed on the large muon sample. In applying these filters it has been assumed that a muon track of more than a metre would definitely be reconstructed. It is also assumed that any signatures observed within one drift window of such a track would not be studied in a nucleon decay search, as there would be doubt as to the authenticity of the signal. Given that the total rate of muons through the active volume is 0.053 Hz, and that the drift time is a few ms, ignoring all times where any track from a cosmogenic muon is present results in less than 0.1% dead time. The dead time associated with ignoring events with muon

¹ tracks of more than 1 m is clearly less than this. This fraction of dead time is assumed to
² be acceptable. Filtering out events where there are no energy depositions in the detector is
³ clearly acceptable, as there are no energy depositions which could mimic a nucleon decay
⁴ signature.

⁵

⁶ After applying this series of cuts, 98.12% of the initial muon sample are removed, mean-
⁷ ing that the initial sample of 2×10^9 muons is reduced to around 4×10^7 muons. This is a
⁸ much more reasonable sample size to store on disk, and to perform analyses on. It is upon
⁹ this reduced sample of muons that the cosmogenic background analyses are performed. As
¹⁰ discussed in Section 2.4.2, the proton decay channel of $p \rightarrow K^+ + \bar{v}_e$ is referred to as the
¹¹ 'Golden Channel' in LAr, this analysis is discussed in [171]. The related decay of a neutron
¹² in the decay $n \rightarrow K^+ + e^-$ is discussed here. The theoretical motivation for this channel was
¹³ briefly discussed in Section 1.2.

¹⁴

¹⁵ 6.3.1 Cosmogenic background to the $n \rightarrow K^+ + e^-$ decay channel

¹⁶ As shown in Table 2.3, the predicted sensitivity that DUNE will have to this channel is much
¹⁷ better than that of Super-K. As a result, it is an interesting decay mode to study. As discussed
¹⁸ in Section 1.2.1, the cosmogenic background to nucleon decay is predominantly caused
¹⁹ by neutral particles, such as a K^0 , entering the detector volume, and interacting relatively
²⁰ far from the detector edges. This is particularly true for the 'Golden Channel,' as shown
²¹ in Figure 1.2, but it also holds for other channels. Events like this are the main cause for
²² concern when eliminating all cosmogenic backgrounds. As mentioned in Section 1.2.1, it is
²³ difficult to separate a K^+ from a K^- in a LArTPC, and so any charged kaon is considered a
²⁴ background in the analysis which is presented in this thesis.

²⁵

²⁶ The analysis presented in this thesis has been performed on Monte Carlo truth informa-
²⁷ tion, and so does not contain any reconstructed quantities. Studies involving hit and track
²⁸ reconstruction are in progress [174], though they will not be discussed here. As Monte Carlo
²⁹ truth information has been used, perfect particle identification (PID) has been assumed. There
³⁰ was also no smearing of the energies, locations, or trajectories of any simulated particles,
³¹ meaning that it is assumed that all deposited charge will be reconstructed, and that the
³² detector characterisation is perfect. This is something which will need to be refined in future
³³ analyses, and will be taken into account when the analysis progresses to use reconstructed
³⁴ quantities, as discussed in Section 6.3.4.

³⁵

As is the case with the 'Golden Channel,' the final state of the decay contains a single charged kaon, and so events which do not contain a kaon track can be immediately discounted. There is also an electron in the final state of the decay, and so this means that events which do not also contain an electron can be discounted. In a nucleon decay event, the kaon and electron produced in the final state will have a common vertex, and so the requirement that the two particles have a common vertex can also be applied. Other constraints that are applied to eliminate background events are; a cut on external muon track length in the active LAr, a cut on depositions near the detector edges, and criteria about the distribution of deposited energy. The criteria about the distribution of deposited energy are found by considering a sample of simulated neutron decay events, and are discussed in Section 6.3.3. These cuts, applied sequentially, are outlined below:

- The event contains energy depositions due to kaons and due to electrons.
- The event contains at least one kaon track, and at least one electron track/shower.
- The event contains a single kaon track, and a single electron track/shower.
- No muon travels more than 20 cm in the active detector volume.
- The event has no energy depositions within 2 cm of the detector edges.
 - This is changed to a maximum of 10 MeV of energy deposited within 2 cm of the detector edge, for reasons which will be discussed in Section 6.3.2.
- The kaon and electron share a common vertex, defined as:
 - The kaon and electron tracks being separated by no more than 5 cm.
 - If the kaon and electron tracks are separated by more than 5 cm, then the point of closest approach between the two extrapolated tracks is less than 2 cm.
- The energy depositions in the event are within the ranges expected from a nucleon decay event. This is explained in Section 6.3.3, but the energies considered are summarised below:
 - The energy directly deposited by the kaon and its secondaries, excluding its decay products.
 - The energy deposited by the kaon decay products and any of their secondaries.
 - The energy directly deposited by the electron and its secondaries.
 - The energy deposited near the shared kaon and electron vertex.

¹ – The energy deposited in the detector which does not fit any of the above criteria.

² When performing the analysis it is important to be able to trace the particle ancestry.
³ This is so that energy depositions in the detector can be properly assigned to the relevant
⁴ particles, as cuts are applied. For example, a μ^+ is often produced when a K^+ decays at
⁵ rest, and this muon may travel more than 20 cm. However, the cut on muon track length
⁶ should not be applied to this muon as it was produced by the decay of the kaon. Similarly,
⁷ as the kaon interacts in the detector secondary particles will be produced, which will be
⁸ reconstructed as tracks coming off the main kaon track. The initial kinetic energy of the
⁹ kaon can only be determined by summing the energy depositions due to these secondary
¹⁰ particles, and the energy depositions due to the kaon itself. Correctly calculating the initial
¹¹ kaon kinetic energy is critical when determining if an event is a nucleon decay event. The
¹² reason for this is that nucleon decay events have very specific energy spectra, and so being
¹³ able to correctly assign the ancestry of energy depositions is vitally important. The same
¹⁴ is true for the electron energy, which is calculated by tracing the ancestry of the particles
¹⁵ produced in the EM shower which it produces back to the electron.

¹⁶

¹⁷ As no reconstruction has been performed, the tracks referred to here are different from
¹⁸ those in Chapters 4 and 5. The definition of a track used here, is that the particle in question
¹⁹ has energy depositions, on simulated wires, which are directly associated with it. These
²⁰ simulated wires are not the same as the wires which have been considered in Chapter 4,
²¹ as the simulated signals have not been digitised. This distinction is important, as it allows
²² the energy depositions directly from GEANT4 to be used, whilst also allowing for LArSoft
²³ methods concerning whether depositions are within TPC boundaries to be utilised.

²⁴

²⁵ The simulated electrons may begin showering immediately, or they may produce a short
²⁶ “track like” segment before beginning to shower. To ensure that every electron shower can be
²⁷ identified, electrons are not required to produce a short “track like” segment. This means that
²⁸ all electrons are assumed to begin showering immediately, and it is also assumed that all of
²⁹ the energy in the shower can be identified as coming from a single electron. This definition
³⁰ of shower energy is the one that is used when the showering algorithms are developed in
³¹ LArSoft. It is hoped that when DUNE begins taking data the showering algorithms will be
³² able to achieve this level of energy reconstruction.

³³

³⁴ When calculating the distance between the start of the kaon track, and the start of the
³⁵ electron track/shower, the energy depositions whose locations are closest to the Monte Carlo
³⁶ truth start points of the particles are used. For particles which are produced within the active

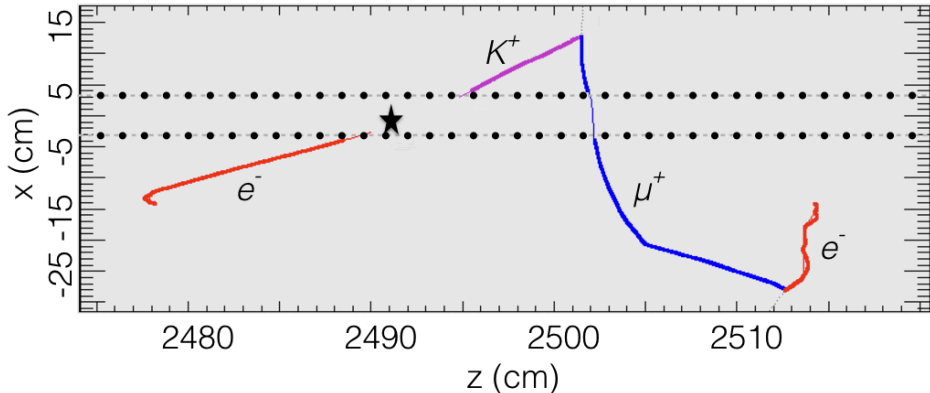


Fig. 6.6 A simulated $n \rightarrow K^+ + e^-$ decay which occurred in a gap between TPCs. The path of the kaon produced in the decay is shown as a purple line. The path of the muon, produced by the decay of the kaon, is shown as a blue line. The paths which the electrons in the event took are shown as red lines. The electron on the left of the figure is the electron produced in the neutron decay, whilst the one on the right of the figure, is produced by the decay of the muon. The thin coloured lines show track segments which were in uninstrumented parts of the detector, such as gaps between TPCs and APAs. The dotted black lines show the edges of the TPCs, and the black star shows the location at which the decay occurred. The distance between the first kaon energy deposition, and the first electron energy deposition, is found to be 10.7 cm. However, when the kaon and electrons tracks are extrapolated towards the true start position, the point of closest approach (PoCA) between the two tracks is found to be 0.67 cm. This shows that they do in fact have a common vertex, despite the large separation of the start points.

volume, these locations generally correspond to the Monte Carlo truth start positions, though this is not always the case. For example, if a particle is created in the gap between two TPCs, then there will be no charge collected until it enters the active volume. This will result in the measured start position to be shifted from the true generation point. This shift can prove troublesome when considering decay events, as if the decay occurred in the centre of an APA, then it is likely that the kaon and electron would deposit energy on opposite sides of the APA. This could cause the depositions to be separated by over 5 cm, as this is the width of the APAs. However, if the tracks are propagated backwards, towards their true start point, it should still be possible to determine that they had a common vertex. An example of a simulated decay event where this happens is shown in Figure 6.6.

In order for a kaon track, and an electron shower, to be considered to share a common vertex, the separation between the start of the kaon track, and the start of the electron shower, must be no more than than 5 cm. A maximum separation of 5 cm is used, as, if the two particles are produced in the centre of a TPC, a gap of 5 cm would require no energy de-

¹ positions to be collected over approximately 10 collection wires. This is assumed to be
² unlikely during data taking, and cannot happen in the simulations considered here, as Monte
³ Carlo truth information is used. As shown by Figure 6.6, however, it is possible for the
⁴ kaon and electron produced in a signal event to be separated by more than 5 cm. To prevent
⁵ events such as this being missed, a second criteria is applied to events with large separations.
⁶ This criteria is that the “Point of Closest Approach” (PoCA) between the two particles,
⁷ found by extrapolating the kaon track and the electron shower, forwards and backwards,
⁸ is less than 2 cm. This is the same PoCA calculation which was made in Section 6.1.2,
⁹ and it means that events such as the one shown in Figure 6.6 are still identified as signal events.

¹⁰

¹¹ The fiducial cut is only applied to the outer edges of the cryostat, as if it were done
¹² with respect to the edge of every TPC in the far detector the loss of volume would be non-
¹³ negligible. This means that the event shown in Figure 6.6 would not fail the fiducial cut, as
¹⁴ the decay occurred over 6 m away from the edge of the detector, but happened to be in a gap
¹⁵ between two TPCs. The need for a fiducial cut is two fold, firstly the vast majority of cosmi-
¹⁶ cally induced events in the detector will have a charged particle which enters the detector.
¹⁷ Performing a fiducial cut will remove all of these events, and will then mean that the only
¹⁸ cosmic background events which can mimic a signal event would involve either a significant
¹⁹ amount of charge being missed, or a neutral particle entering the detector, and interacting
²⁰ relatively far from the detector walls. Secondly, in order to calculate the kinetic energies of
²¹ the particles produced in the nucleon decay, and also to perform particle identification, they
²² must be fully contained within the detector. As such, if one of the particles produced in the
²³ nucleon decay escapes the detector then its kinetic energy cannot be determined accurately,
²⁴ and if it is the kaon, or its decay products, then the particle cannot be identified using the
²⁵ method discussed in Section 4.4. This will also affect any particles which stop in the gaps
²⁶ between TPCs, as the end point will not be reconstructed, though PID may still be possible
²⁷ as the end point can be estimated. A fiducial cut of 2 cm is used, as the loss of active volume
²⁸ which this causes is negligible in the DUNE FD. A 2 cm fiducial cut also ensures that a
²⁹ significant amount of charge would have to be missed for a particle which enters/escapes the
³⁰ detector to be incorrectly identified as being contained within the detector.

³¹

³² Once both the ancestry of energy depositions in the simulation, and the initial kinetic
³³ energies, have been correctly accounted for and calculated, it is possible to observe the distri-
³⁴ bution of background events, as the cuts outlined above are applied. The energy distribution
³⁵ of background events surviving the application of sequential cuts is shown in Figure 6.7.
³⁶ The energy distribution of background events per MeV of energy deposited, surviving the

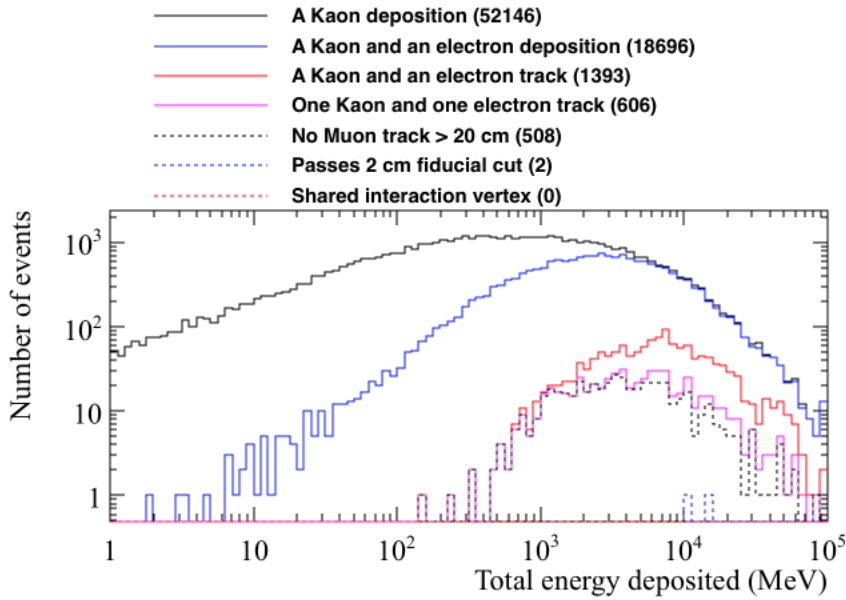


Fig. 6.7 The energy distribution of background events surviving the application of sequential cuts. The total energy deposited in the detector is plotted on the x axis. A sample of 2×10^9 muons, representing 401.6 years of detector for a single FD module is shown.

application of sequential cuts is shown in Figure 6.8. This distribution is obtained by dividing the number of events within an energy bin by the bin width.

From Figures 6.7 and 6.8, it can be seen that there are no background events which could mimic a decay signature as no events survive the application of all cuts. This corresponds to a limit of the background rate of less than 0.44 events/Mt/year at the 90% confidence level, using double sided errors [25] and a fiducial mass of 13.8 kt to give an exposure of 5.542 Mt·year.

It is interesting to observe the effect that relaxing some of the cuts has on the background rate. For example, the cuts after the requirement that there be at least one kaon track and at least one electron shower in the event, could be relaxed. This is shown in Table 6.9, where the later cuts have been applied in isolation to observe their effectiveness.

The effectiveness of the fiducial cut is clearly apparent from Table 6.9, as it removes all but 5 of the 1393 events where there is both a kaon track and an electron shower. The requirement that the kaon track and electron shower share a common vertex is also seen to be very effective at removing background events, as only 64 of the 1393 meet this condition.

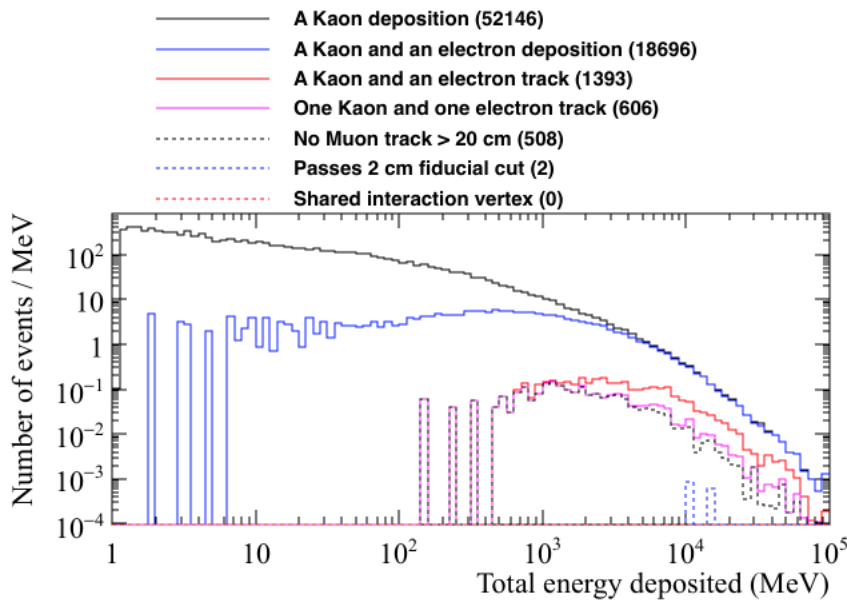


Fig. 6.8 The energy distribution of background events per MeV of deposited energy surviving the application of sequential cuts. The total energy deposited in the detector is plotted on the x axis. This distribution is obtained by dividing the number of events within an energy bin by the bin width. A sample of 2×10^9 muons, representing 401.6 years of detector for a single FD module is shown.

Table 6.9 The number of events which could mimic a $n \rightarrow K^+ + e^-$ decay, when cuts are applied in isolation. Cuts are applied after it is required that the event contains at least one kaon track and at least one electron shower. It is found that 1393 events have at least one kaon track and at least one electron shower, this is shown in the top row of the table. The fiducial cut of 2 cm is seen to remove almost all of the events considered.

Cut that is applied	Num. events surviving cut	% surviving
At least one kaon track, and electron shower	1393	100
Only one kaon track, and only one electron shower	606	43.5
No muon track that is longer than 20 cm in length	1223	87.8
No energy depositions within 2 cm of detector edge	5	0.359
The kaon and electron share a common vertex	64	4.59

When the cuts are no longer applied in isolation, but are instead applied in a different order to that used when producing Figures 6.7 and 6.8, it is found that in only 15 of the 606 events that have a single kaon track and a single electron shower, would the kaon and electron be considered to have a common vertex. When the additional constraint of there not being a muon with a track length of more than 20 cm present in the event 10 of the remaining 15 events background events would still not be removed. This shows that the only way to remove all of the background events is to apply all of the cuts which have been developed, including the fiducial cut.

6.3.2 Signal events in the $n \rightarrow K^+ + e^-$ decay channel

It is important to confirm that the cuts developed to reject cosmic backgrounds do not adversely affect the identification of nucleon decay events. For this reason, a sample of 10,000 neutron decay events in the DUNE far detector were generated using GENIE [105]. Neutron decays are generated at random positions within the detector volume, and so it is possible that the decay occurs in the gaps between TPC volumes, as shown in Figure 6.6, or near the edge of the detector, as is shown in Figure 6.9. However, many of the neutron decay events are fully contained within a single TPC, as shown by Figure 6.10.

The analysis performed on the cosmogenic background was primarily designed to reject background events, whilst also attempting to not use cuts which would also affect signal efficiency. Therefore, it is hoped that the loss of signal events will be minimal. When running the analysis on the simulated signal events, the same definitions for tracks, showers, and the ancestry of particles are used, as well as the same cuts that were outlined in Section 6.3.1.

The energy distribution of the signal events surviving the application of the sequential cuts is shown in Figure 6.11, this is the equivalent of Figure 6.7 for the cosmogenic background sample. The energy distribution of signal events per MeV of energy deposited, surviving the application of sequential cuts is shown in Figure 6.12, this is the equivalent of Figure 6.8 for the cosmogenic background sample. As before, this distribution is obtained by dividing the number of events within an energy bin by the bin width.

When comparing Figures 6.11 and 6.12 with Figures 6.7 and 6.8, the most obvious difference is that when considering the nucleon decay events, the total energy deposited in the detector never exceeds 1 GeV, whilst in the cosmogenic background sample, the energy deposited in the detector frequently exceeds 1 GeV. This is something which one would

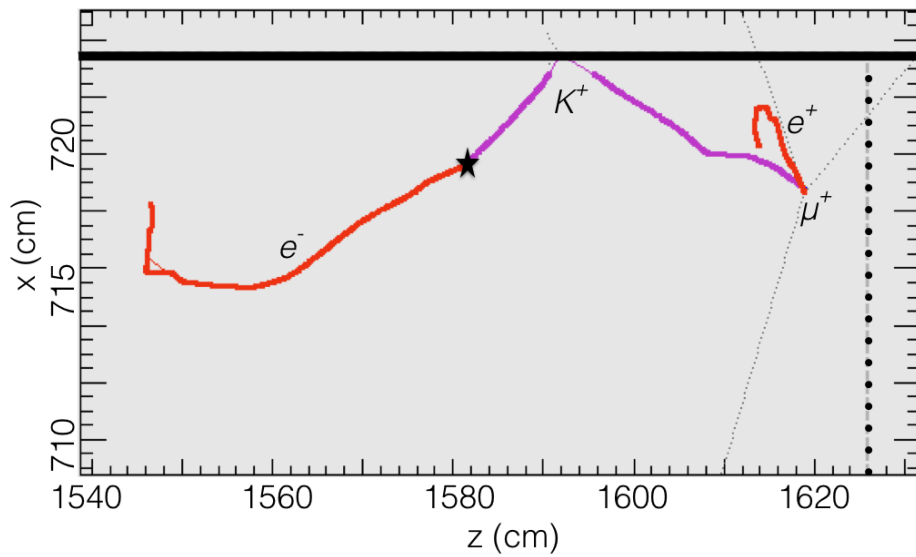


Fig. 6.9 A simulated $n \rightarrow K^+ + e^-$ decay which occurred near the edge of the detector volume. The path of the kaon produced in the decay is shown as a purple line. The path of the muon, produced by the decay of the kaon, is shown as a blue line, though it is very short and so barely visible. The paths which the electrons in the event took are shown as red lines. The electron on the left of the figure is the electron produced in the neutron decay, whilst the one on the right of the figure, is produced by the decay of the muon. The thin grey lines show spallation neutrons. The thin coloured lines show track segments which were in uninstrumented parts of the detector, such as the edge of the active volume. The solid black line shows the edge of the detector. The dotted black lines show the edges of the TPCs, and the black star shows the location at which the decay occurred. It can be seen that though most of the energy depositions are contained within the detector, the kaon passes very close to the edge of the detector, and so some of its charge is not reconstructed. The proximity of the decay to the detector walls causes there to be a large amount of charge deposited near the edge of the detector.

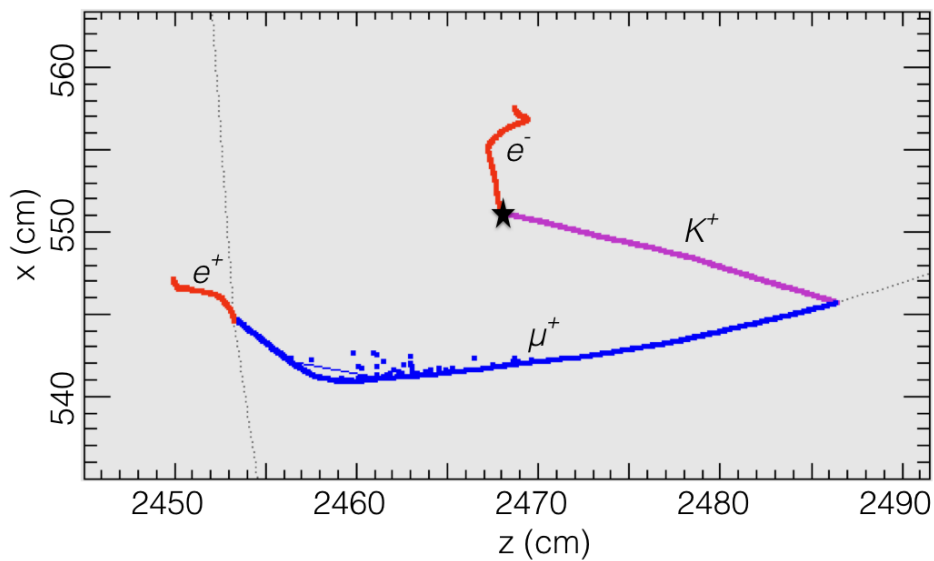


Fig. 6.10 A simulated $n \rightarrow K^+ + e^-$ decay which is fully contained in a single volume. The path of the kaon produced in the decay is shown as a purple line. The path of the muon, produced by the decay of the kaon, is shown as a blue line. The paths which the electrons in the event took are shown as red lines. The electron at the top of the figure is the electron produced in the neutron decay, whilst the one at the bottom left of the figure, is produced by the decay of the muon. The thin grey lines show spallation neutrons. The black star shows the location at which the decay occurred. It can be seen that all of the deposited charge is contained within a single TPC.

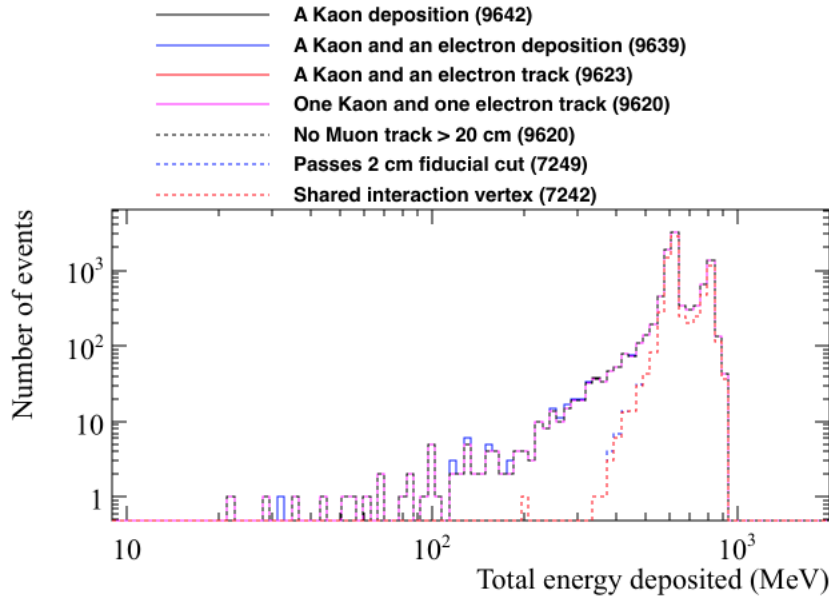


Fig. 6.11 The energy distribution of signal events surviving the application of sequential cuts in the $n \rightarrow K^+ + e^-$ channel. The total energy deposited in the detector is plotted on the x axis.

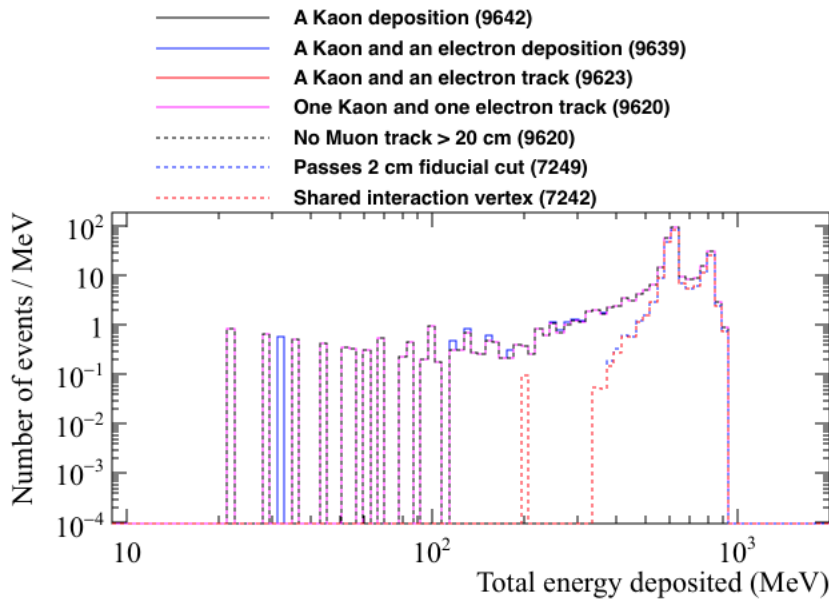


Fig. 6.12 The energy distribution of signal events per MeV of deposited energy surviving the application of sequential cuts. The total energy deposited in the detector is plotted on the x axis. This distribution is obtained by dividing the number of events within an energy bin by the bin width.

Table 6.10 The most common decay modes of charged kaons, and their probabilities [25]. The decay modes shown are with reference to K^+ , though the decays of K^- are the charge conjugations of these decays.

Decay mode	Measured probability (%)
$K^+ \rightarrow \mu^+ + \nu_\mu$	63.56 ± 0.11
$K^+ \rightarrow \pi^+ + \pi^0$	20.67 ± 0.08
$K^+ \rightarrow \pi^+ + \pi^+ + \pi^-$	5.583 ± 0.024
$K^+ \rightarrow \pi^0 + e^+ + \nu_e$	5.07 ± 0.04
$K^+ \rightarrow \pi^0 + \mu^+ + \nu_\mu$	3.352 ± 0.033
$K^+ \rightarrow \pi^+ + \pi^0 + \pi^0$	1.760 ± 0.023

expect, as the simulated neutrons decay at rest, and so have a total energy of less than 1 GeV, meaning that there cannot be more than 1 GeV deposited in the detector. This is in stark contrast to the cosmogenic background, where the primary muons being generated have a mean energy of 283 GeV, as shown in Table 6.8. This means that many events will deposit significant amounts of energy in the detector, even if the primary muon misses the detector volume.

A striking feature of Figures 6.11 and 6.12, is the double peaked structure of the total energy deposited in the detector. This can be attributed to the amount of energy from the kaon decay which is not reconstructed. The relative strengths of these structural features is due to the various probabilities of the kaon decay modes. Some of the more common decay modes are shown in Table 6.10, along with their probabilities. The amount of energy which is reconstructed from the particles produced by the decay of the kaon is shown in Figure 6.13.

As can be seen in Table 6.10, the most common decay mode for the kaon involves the production of a ν_μ , which will leave the detector without interacting. This will mean that a significant proportion of the kaon rest mass energy will not be seen, as the kaon is assumed to decay at rest. Then the most likely amount of energy deposited by the kaon decay products is around 200 MeV. The second most likely decay mode is also a 2-body decay, though some of the kaon rest mass energy will not be seen when the π^+ decays. This is why the second peak at 400 MeV is less than the rest mass of the kaon. Neutrinos are also present in many of the other decay modes, and so will also have large amounts of missing energies, whilst the 3-body decay modes will produce particles which have a continuous distribution of energies. These decay modes cause the energy deposited by the kaon decay products to be a continuous distribution, with two large peaks at roughly 200 MeV and 400 MeV, due to the two body

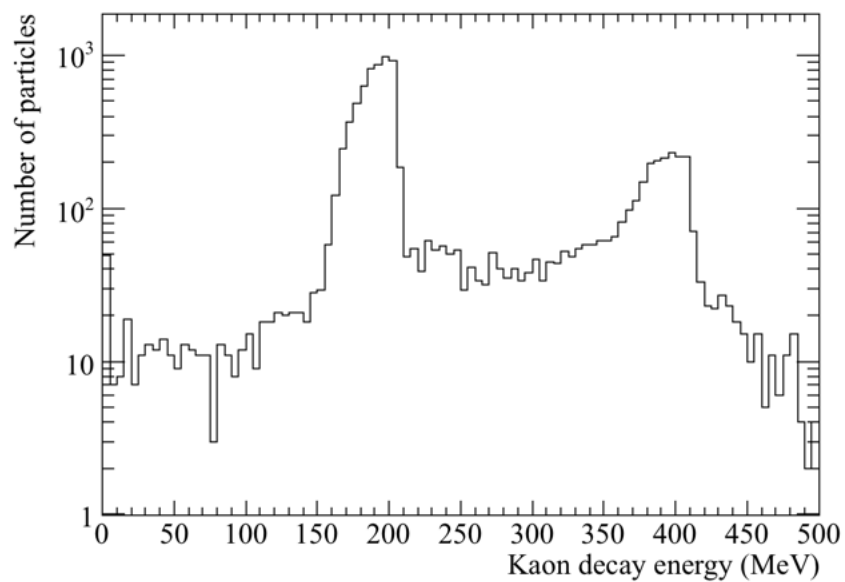


Fig. 6.13 The number of events as a function of the energy deposited by the kaon decay products. The energies deposited due to the $K^+ \rightarrow \mu^+ + \nu_\mu$ and $K^+ \rightarrow \pi^+ + \pi^0$ decay channels can be seen in the peaks at roughly 200 MeV, and 400 MeV, respectively. The underlying continuous distribution of depositions is caused by the 3-body decays shown in Table 6.10.

decays illustrated above.

The initial cuts, requiring that both a kaon track and an electron shower are observed in the decay, show that there are occasions when either the kaon, or the electron, do not deposit energy in the detector. This affects very few events, though an example of one such event is shown in Figure 6.14, where it can be seen that the kaon decayed before entering the active volume, and so no track was found for it. It would be very difficult to identify this event as a signal event, as the presence of the kaon could only be inferred from the muon originating from the gap between the APAs, and the energy deposited by the kaon itself will not be reconstructed. Further compounding the identification of this event as a signal event, is the fact that the electron produced in the nucleon decay scatters back into the gap between the APAs. This means that a significant amount of the rest mass energy of the neutron would not be reconstructed.

The number of events which are removed by the fiducial cut is concerning, as when it is considered in conjunction with other cuts it removes almost 25% of events. This suggests that the cut is too strict. The reason for this is two fold. Firstly, protons and neutrons are emitted from the nucleus in many of the simulated decays, and whilst the protons produced will create relatively short tracks, which are connected to the decay vertex, the neutrons will travel large distances, and cause energy depositions which are far away from the decay vertex. The faint grey dashed lines, which can be seen in Figure 6.14, show the spallation neutrons produced in the decay. None of the figures shown here contain spallation protons, but if they were present, they would be shown as additional purple lines originating from the decay vertex. In a large number of events energy depositions from the spallation neutrons are causing events to fail the “no energy depositions within 2 cm of the detector edge” cut by depositing very small amounts of energy close to the detector walls. Secondly, though the decays are randomly distributed in the active volume of the detector, some of these decays will occur close to the detector walls. For example, over 500 (2,500) of the neutron decays occur within 30 (100) cm of the detector walls. An example of one such event is shown in Figure 6.9, where the kaon produced in the decay deposits a significant amount of energy close to the edge of the detector. As a result, it is likely that this cut needs to be relaxed to instead be a cut on the amount of energy deposited within 2 cm of the detector edge. Figure 6.15 shows the amount of energy deposited within 2 cm, 5 cm, and 10 cm of the detector edges, for the simulated nucleon decay events (Figure 6.15a), and the cosmogenic background events (Figure 6.15b).

1
2
3
4
5
6
7
8
9
10
11
12
13
14
15
16
17
18
19
20
21
22
23
24
25
26
27
28
29
30
31
32
33
34
35
36

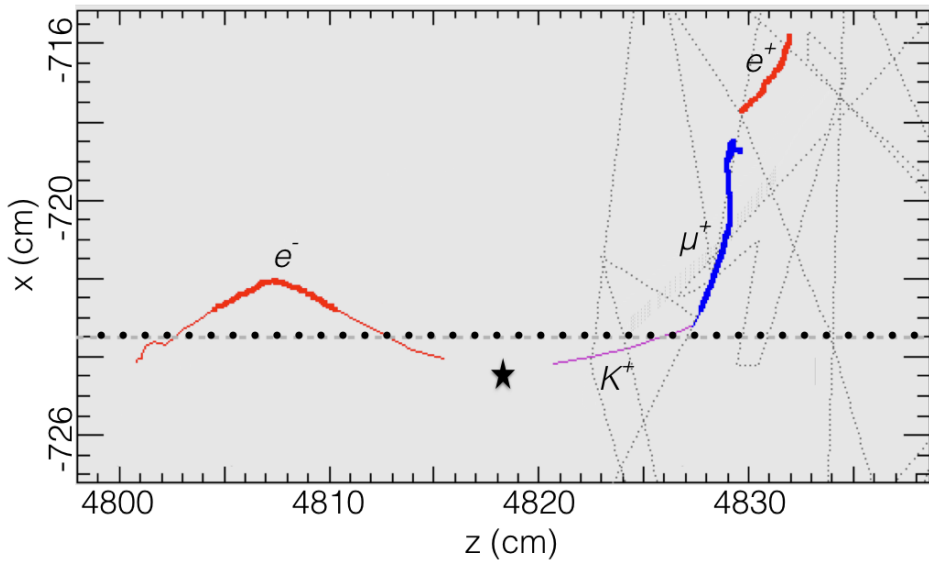
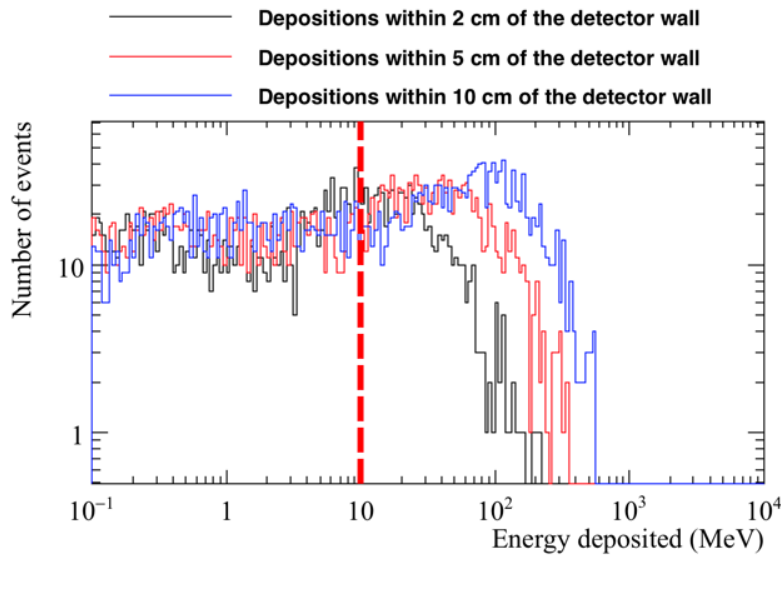
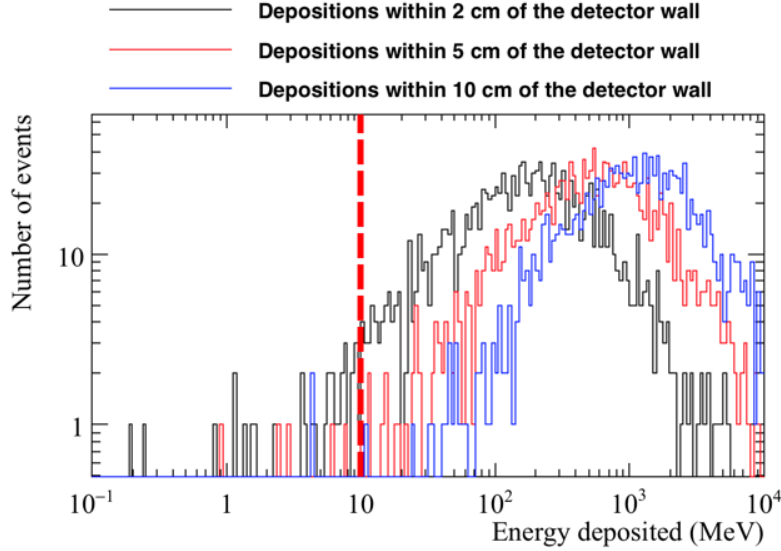


Fig. 6.14 A simulated $n \rightarrow K^+ + e^-$ decay where the kaon did not deposit any energy in the active volume. The path of the kaon produced in the decay is shown as a purple line. The path of the muon, produced by the decay of the kaon, is shown as a blue line. The paths which the electrons in the event took are shown as red lines. The electron on the left of the figure is the electron produced in the neutron decay, whilst the one on the right of the figure, is produced by the decay of the muon. The thin coloured lines show track segments which were in uninstrumented parts of the detector, such as gaps between TPCs and APAs. The dotted black lines show the edges of the TPCs, and the black star shows the location at which the decay occurred. It can be seen that the kaon decayed before it entered the active volume of the detector, and so no track was found for it. A significant portion of the distance which the electron from the decay travelled was also outside the active volume of the detector.



(a) The nucleon decay events.



(b) The cosmogenic background events.

Fig. 6.15 The number of events, as a function of the energy deposited within 2 cm, 5 cm, and 10 cm of the detector edges. Top: energy depositions for the simulated neutron decay events. Bottom: energy depositions for the simulated cosmogenic background events. The histograms are filled after the cut requiring that there is at least one kaon track and at least one electron shower in the event, is applied. As such, the histograms are filled with 9,623 and 1,393 events for the top and bottom histograms respectively. The dashed red line shows the effect of a cut on the energy deposited of 10 MeV. This cut will remove all events which are to the right of the line.

1 As can be seen from Figure 6.15, the amount of energy deposited near the detector edges
2 is very different in the nucleon decay, and cosmogenic background events. As such, they can
3 be relatively cleanly separated. In many of the signal events less than 0.1 MeV of energy is
4 deposited near the detector edge, and so these events are not shown here. It can be seen that in
5 some signal events there are significant energy depositions near the detector edge. Figure 6.9
6 shows an event where the kaon and electron shower deposit large amounts of energy near the
7 detector edge. The energies deposited near the detector edge by the background events is
8 very large, and is generally due to the presence of large showers which enter the detector.
9

10 A cut demanding that there should be no more than 10 MeV of energy deposited within 2
11 cm of the detector edge is used. This cut is designed to preserve as many of the simulated
12 signal events as possible, whilst rejecting as many background events as possible. This
13 cut removes only 683 of the 9,623 signal events, whilst only 39 out of the 1,393 cosmic
14 background events meet this requirement. Whilst this does mean that the fiducial is less
15 effective at removing background events from the cosmic sample, it does not cause the huge
16 loss of signal events which seen when using the hard cut of “no energy depositions within
17 2 cm of the detector edge.” It is also important to remember that the other cuts will still be
18 applied to these 39 events, as the fiducial cut is not applied in isolation. As will be seen in
19 Figure 6.17b none of the muon-induced background events survive the application of all cuts.
20

21 The definition used to decide if the kaon track and the electron shower share a common
22 vertex seems to be a reasonable requirement, as almost all of the signal events satisfy this
23 definition. Figure 6.16 shows the distance between the start of the kaon track and the start
24 of the electron shower in signal events. It can be seen that the separation between the two
25 particles is very small (<0.1 cm) in most events. However, there are some events where the
26 separations are very large (>10 cm). As discussed earlier, the decays in these events occur in
27 the gaps between TPCs, such as that shown in Figure 6.6. When the requirement that the
28 kaon track and the electron shower have a PoCA of less than 2 cm is then applied to these
29 events, most of them are then seen to have a common interaction vertex. For example, this is
30 found to be the case for the event shown in Figure 6.6. However, in some events the kaon
31 track and the electron shower are still not found to have a common interaction vertex. Hand
32 scanning shows that the particles in these events undergo scattering before entering the active
33 volume, and so by the time that energy depositions occur their trajectories are no longer
34 closely aligned. This causes the PoCA to be larger than 2 cm, and so they are not identified
35 as a signal event.

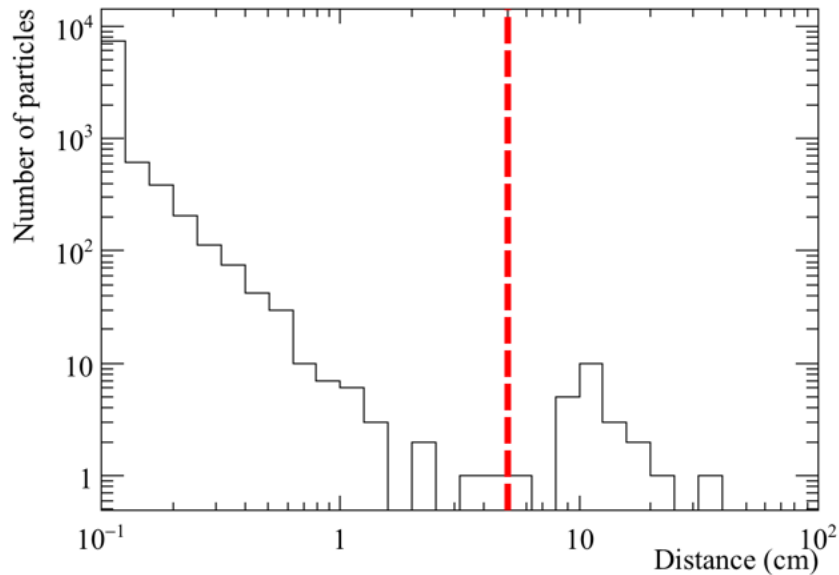
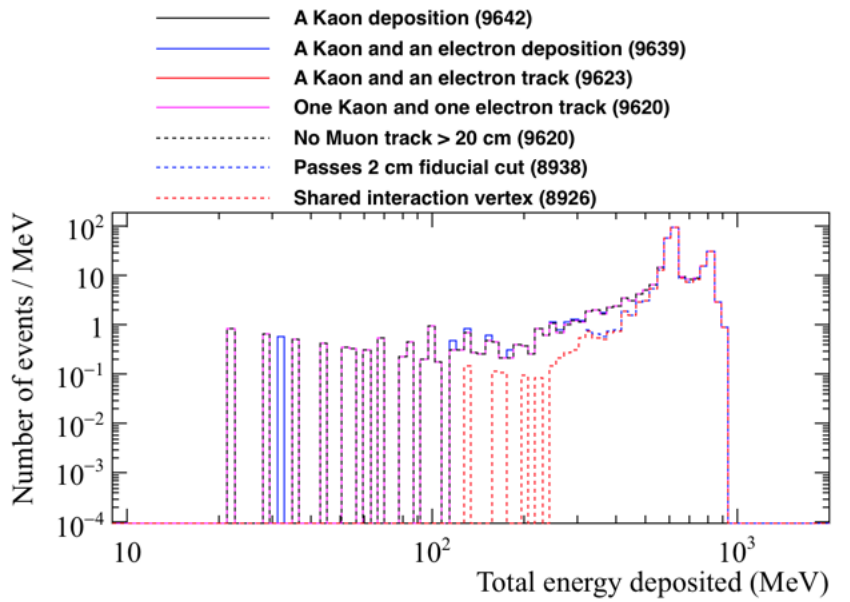


Fig. 6.16 The separation of the kaon and the electron produced in the simulated $n \rightarrow K^+ + e^-$ decays. The dashed red line, drawn at a separation of 5 cm, shows the maximum possible separation a kaon and an electron could have, and still be considered to have a common vertex. A separation of 5 cm is used as this is the separation of the TPCs in the FD.

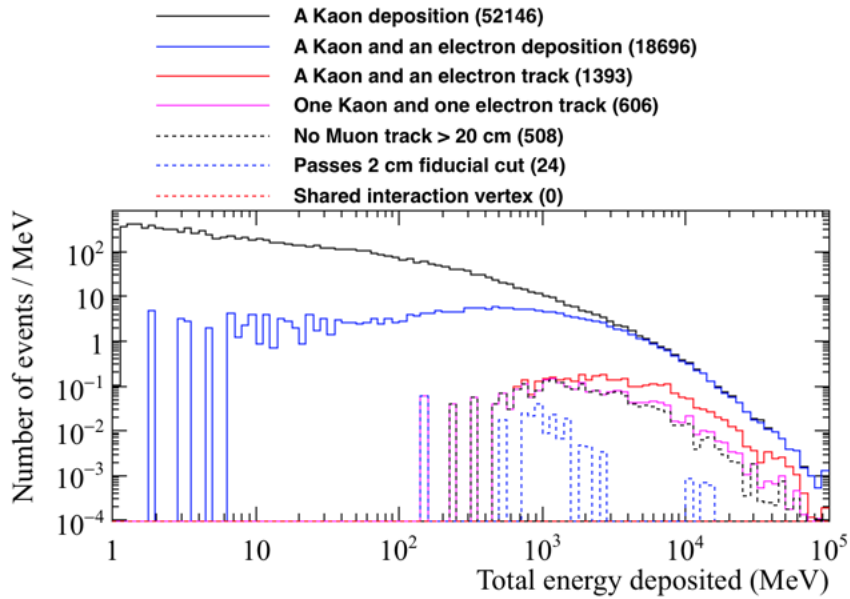
Figure 6.17 shows the energy distributions per MeV of deposited energy for the simulated decay (Figure 6.17a) and cosmogenic background (Figure 6.17b) events, after the fiducial cut is changed to require that there is less than 10 MeV of energy deposited within 2 cm of the detector edge. As before, these distributions are obtained by dividing the number of events within an energy bin by the bin width.

The number of signal events which are removed by the cuts can be seen to be much more reasonable after the fiducial cut is modified, as just 1,074 (10.74%) of the 10,000 signal events are removed as cuts are applied. It is seen that in many of the simulated decay events which fail the cuts, at least one of the kaon, or the electron, are not contained in the active volume of the detector. This means that, either no depositions are found for at least one of the particles (361 events), or there are large energy depositions close to the edge of the detector (682 events).

It can be seen that none of the cosmic background events pass the application of all cuts, though of the 24 events which pass the fiducial cut, only 9 of them deposit less than 1 GeV in the detector. This means that the total energy deposited in the detector is more than the rest



(a) The energy distribution of signal events.



(b) The energy distribution of cosmic background events.

Fig. 6.17 The energy distributions per MeV of deposited energy for the signal and cosmic background events, surviving the application of sequential cuts after the fiducial cut is modified. The total energy deposited in the detector is plotted on the x axis. These distributions are obtained by dividing the number of events within an energy bin by the bin width.

mass of a neutron, and so the event is not consistent with being from the decay of a neutron at rest. Section 6.3.3 will consider the energy deposition distributions of the simulated neutron decay events, to establish additional constraints which can be applied to background events.

6.3.3 Energy constraints on the cosmogenic background to the $n \rightarrow K^+ + e^-$ decay channel

As outlined in Section 6.3.1, it is possible to exclude background events from signal events, using the distribution of energy depositions in the detector. As previously outlined, the energy depositions were split into several categories:

- The energy directly deposited by the kaon and its secondaries, excluding its decay products.
- The energy deposited by the kaon decay products and any of their secondaries.
- The energy directly deposited by the electron and its secondaries.
- The energy deposited near the shared kaon and electron vertex.
- The energy deposited in the detector which does not fit any of the above criteria.

Following the earlier discussions in Section 6.3.1, it should be clear that the energy directly deposited by the kaon corresponds to the sum of all energy depositions, which are due to the kaon or its interaction products. Equivalently, the energy directly deposited by the electron, corresponds to the sum of all energy depositions which are due to the electron as it showers, and any particles created as a result of the shower. The energy deposited by the kaon decay products would include all depositions by the muon and subsequent electron, in the case that the kaon decayed via $K^+ \rightarrow \mu^+ + \bar{\nu}_\mu$, and then the muon decayed via $\mu^+ \rightarrow e^+ + \nu_e + \bar{\nu}_\mu$. The energy deposited near the shared kaon and electron vertex, would primarily consist of energy depositions due to spallation products. These depositions would largely be due to protons, though may also include some depositions due to neutrons too, if they deposited energy near the interaction vertex. Any depositions within 5 cm of either the start of the kaon track, or the start of the electron shower, are considered “near” to the interaction vertex. It is necessary to consider the energy depositions which are close to the start of both particles, because occasionally the particles are separated by the APA gaps, as shown in Figure 6.6. As can be seen from Figure 6.16, the separation between the start of the kaon track and the start of the electron shower, is normally very small. This means that the sum of the

¹ “near” energy depositions, can be considered to be the energy depositions “near” the common
² vertex between the kaon track and the electron shower. The final criteria, of any depositions
³ which do not fit the above description, would largely consist of energy depositions due to the
⁴ spallation neutrons in the decay sample. However, in the cosmic background sample, this
⁵ would include all depositions by muons, pions, and any other particles in the detector which
⁶ are not associated with either the kaon or the electron. In later discussions these depositions
⁷ are generally labelled as “other” energy depositions.

⁸

⁹ In presenting the separation of simulated cosmic background events and simulated neutron
¹⁰ decay events, the important distributions to consider are as follows:

- ¹¹ • The energy directly deposited by the kaon, against the energy directly deposited by the
¹² electron. This is shown in Figure 6.18.
- ¹³ • The energy directly deposited by the kaon, plus the energy directly deposited by the
¹⁴ electron, against the energy deposited near the shared kaon and electron vertex. This is
¹⁵ shown in Figure 6.19.
- ¹⁶ • The energy deposited by the kaon, including decay products, against the energy
¹⁷ deposited in the detector which does not fit any of the other criteria. This is shown in
¹⁸ Figure 6.20.
- ¹⁹ • The energy deposited by the kaon, including decay products, plus the energy directly
²⁰ deposited by the electron, plus the energy deposited near the shared kaon and electron
²¹ vertex, against the energy deposited in the detector which does not fit any of the other
²² criteria. This is shown in Figure 6.21.

²³ Each of these figures will be discussed in turn below. The events in the nucleon decay sample
²⁴ which pass all cuts have been plotted with smaller markers, this is to allow the less numerous
²⁵ events which fail the cuts to be visible.

²⁶

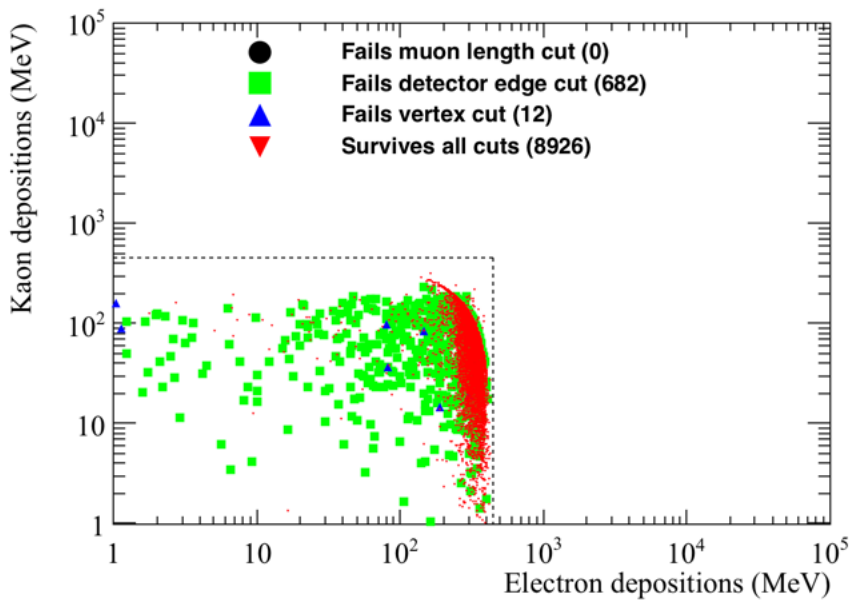
²⁷ Additionally, the figures outlined above have a box in the lower left corner of the plots
²⁸ produced by dashed grey lines. This constitutes the expected energy region where a signal
²⁹ event would lie on the graph, and has been drawn so as to contain as many of the simulated
³⁰ signal events as possible. The expected energy regions are propagated down to 0 MeV on
³¹ both the x and y axis of all figures, and so it is possible for points not drawn here to pass the
³² applied cuts. This is because it is possible for signal events to have no energy identified as
³³ ‘near’ the common interaction vertex, such as the event shown in Figure 6.6. It is also possi-

ble for there to be no energy deposition which would be classed as “other” energy depositions.

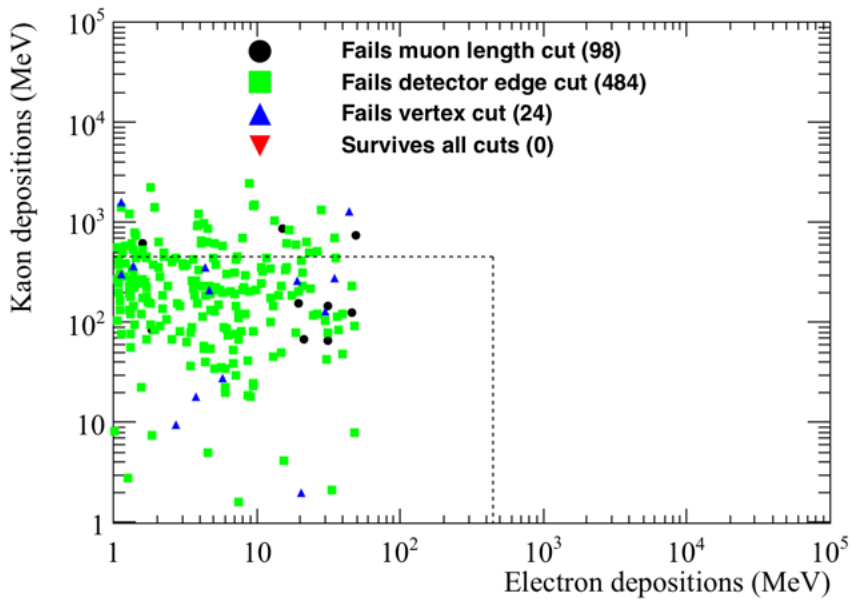
From Figure 6.18, it can be seen that the electron energy distribution in the cosmic background sample, is very different from the one seen in the simulated neutron decay sample. The energies deposited by electrons in the nucleon decay sample are tightly concentrated between ~ 200 and ~ 400 MeV, whilst in the cosmic background sample, the energy deposited by the electron is almost always less than ~ 50 MeV. Many of the electrons in the cosmic background sample deposit less than 1 MeV of energy in the detector, and so are not shown in Figure 6.18b. This is why Figure 6.18b is very sparse despite 606 events being plotted. Realistically, these electrons are unlikely to be reconstructed due to their extremely low energies. From Figure 6.18a, it can be seen that some of the electrons produced in the nucleon decay events also deposit very little energy in the detector, though these events generally fail either the fiducial cut, or the vertex cut. An explanation as to why these events fail the cuts was presented in Section 6.3.2, when considering Figure 6.14.

From Figure 6.19a, it can be seen that as the energy deposited near the kaon and electron vertex increases, the sum of the energy deposited by the kaon and electron decreases. This is reasonable, because, when the spallation protons and neutrons have more energy, the kaon and electron will have less energy. The decrease in the energy deposited by the kaon and the electron, is roughly consistent with the increase in the amount of energy which is deposited near their shared vertex. This means that the sum of the three energies is generally around 450 MeV, as expected from the kinematic calculations shown in Section 1.2.2 where a two body decay was assumed. Though this is no longer valid when 3+ particles are produced, the majority of the rest mass energy of the neutron will be still be measured if the neutron energies are small. This is largely inconsistent with the simulated cosmic background events, where many events have no energy deposited near the shared vertex of the kaon and electron. However, the lack of energy deposited near the shared kaon and electron vertex cannot be used to discriminate against cosmogenic background events, as this is also observed in many simulated nucleon decay events. What can be used to separate cosmic background events from nucleon decay events though, is the sum of the three energy criteria, as it can be seen that this would rarely be around 450 MeV in the cosmic background sample.

Figure 6.20, shows that the sum of all energy deposits attributed to the kaon, against the sum of all energy depositions which are considered to be “other” energy depositions, is very different in the two samples. The total energy deposited in the detector which is attributed to the kaon is found by combining the energy directly deposited by the kaon,

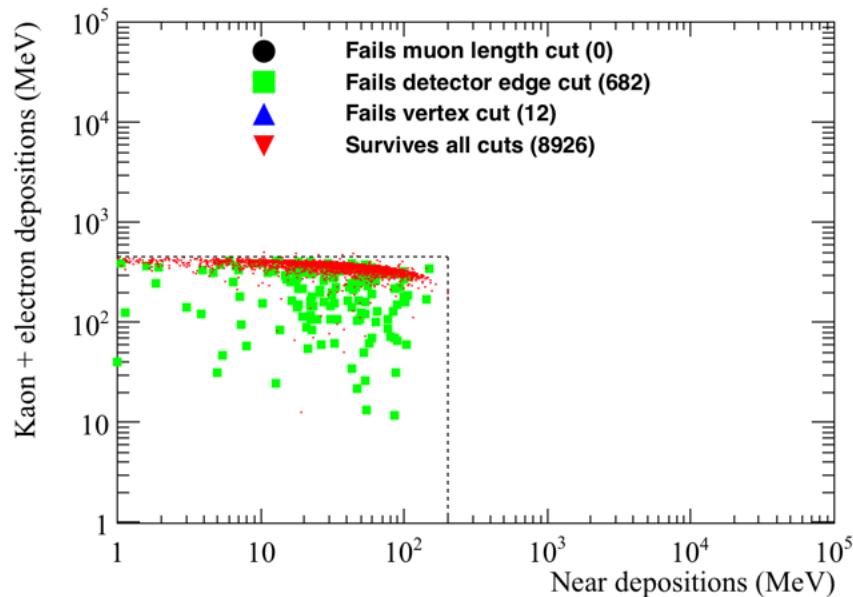


(a) Signal events.

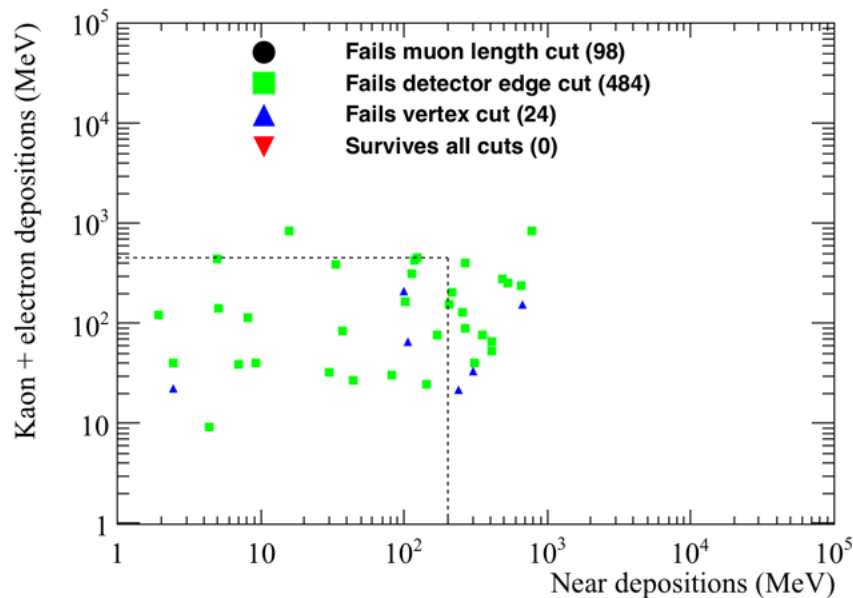


(b) Cosmic background events.

Fig. 6.18 The energy directly deposited by kaons versus the energy directly deposited by electrons, in the simulated nucleon decay (top) and cosmic background samples (bottom). The events failing the application of the muon length (black circle), fiducial (green box) and vertex (blue triangle) cuts, as well as the events passing all cuts (red triangle) are shown. The cuts are those defined at the start of Section 6.3.1.

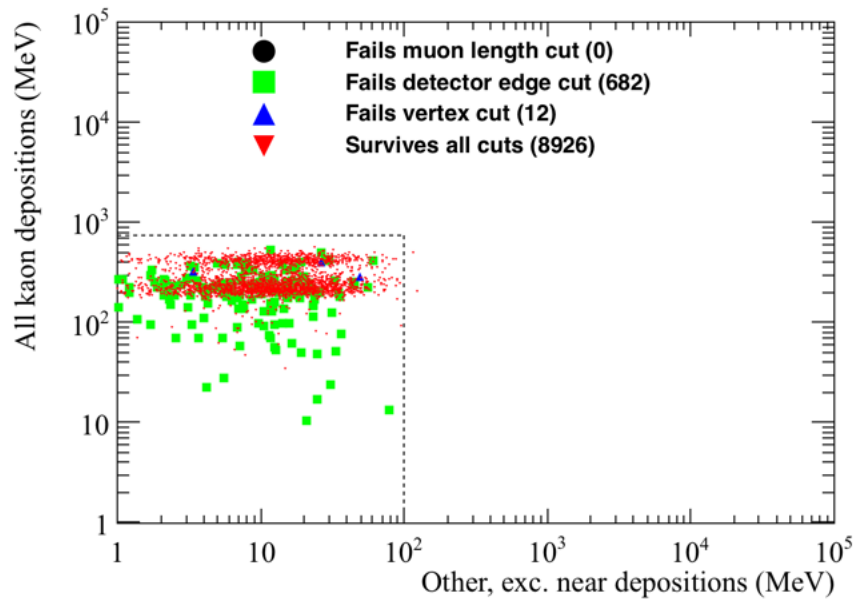


(a) Signal events.

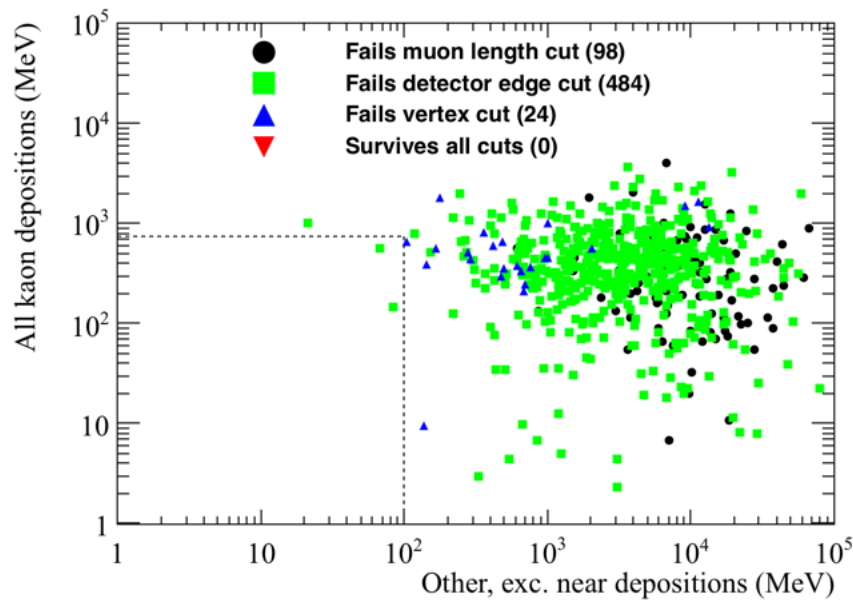


(b) Cosmic background events.

Fig. 6.19 The energy directly deposited by kaons, plus the energy directly deposited by electrons versus the energy deposited near the kaon and electron vertex, in the simulated nucleon decay (top) and cosmic background samples (bottom). The events failing the application of the muon length (black circle), fiducial (green box) and vertex (blue triangle) cuts, as well as the events passing all cuts (red triangle) are shown. The cuts are those defined at the start of Section 6.3.1.



(a) Signal events.



(b) Cosmic background events.

Fig. 6.20 The energy directly deposited by kaons, plus the energy deposited by the kaon decay products versus the energy depositions which do not fit any of the other criteria, in the simulated nucleon decay (top), and cosmic background samples (bottom). The events failing the application of the muon length (black circle), fiducial (green box) and vertex (blue triangle) cuts, as well as the events passing all cuts (red triangle) are shown. The cuts are those defined at the start of Section 6.3.1.

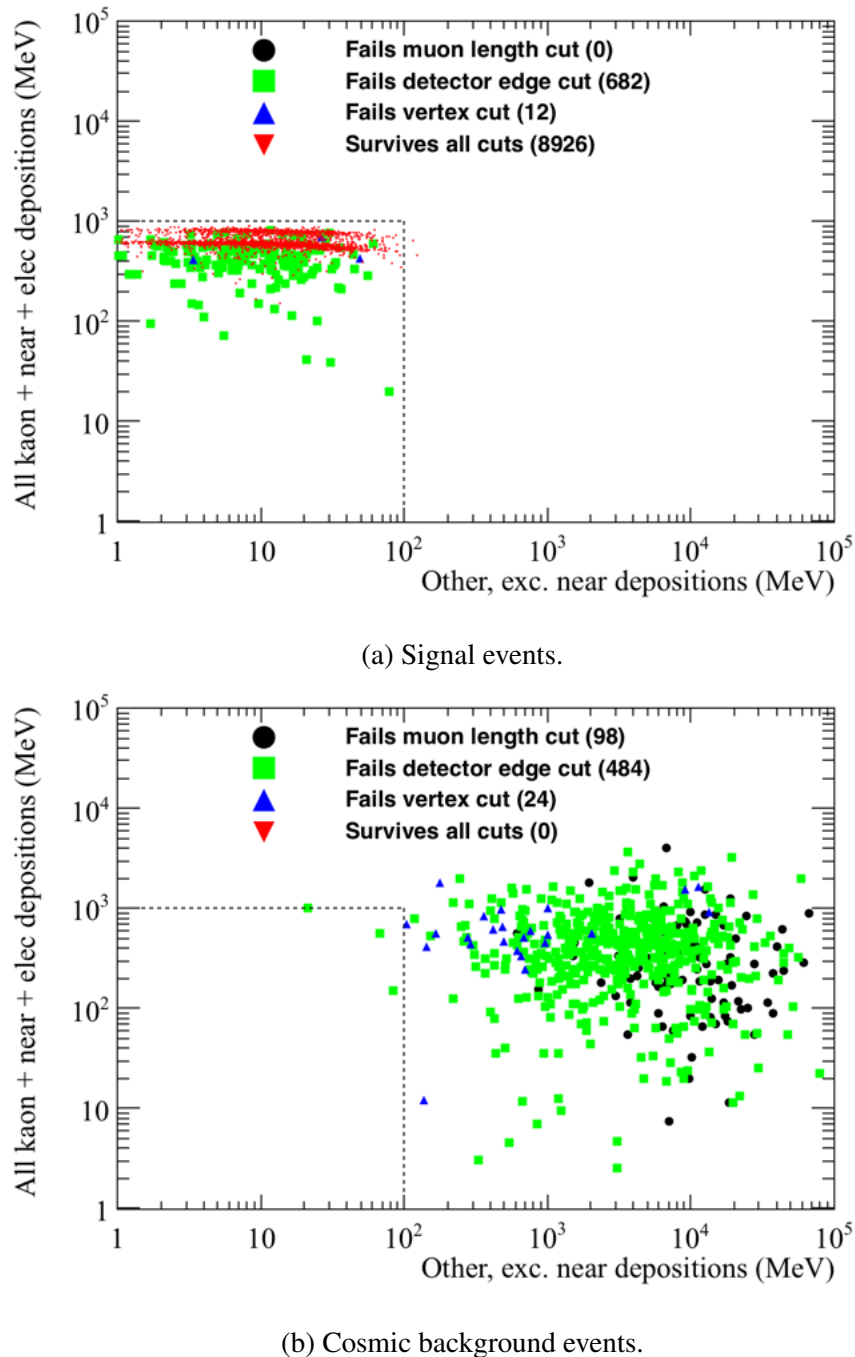


Fig. 6.21 The energy directly deposited by kaons, plus the energy deposited by the kaon decay products, plus the energy directly deposited by electrons, plus the energy deposited near the kaon and electron vertex versus the energy depositions which do not fit any of the other criteria, in the simulated nucleon decay (top) and cosmic background samples (bottom). The events failing the application of the muon length (black circle), fiducial (green box) and vertex (blue triangle) cuts, as well as the events passing all cuts (red triangle) are shown. The cuts are those defined at the start of Section 6.3.1.

1 with the energy deposited by the kaon decay products. This sum is seen to have a banded
2 structure in Figure 6.20a, this is due to the amount of energy from the kaon decay which is
3 not reconstructed, and was discussed when considering Figure 6.13. The difference seen in
4 the cosmogenic background and signal events, is primarily due to the large amount of “other”
5 energy depositions which are seen in the cosmogenic background sample. This is expected,
6 as in muon-induced events many particles may enter the detector, causing energy depositions
7 which are not connected to the kaon track, the electron shower, or their common vertex,
8 should one exist. This gives the most powerful mechanism for the discrimination between
9 signal and background events, as in many background events the “other” energy deposited in
10 the detector will be very large, and will cause the total energy deposited in the detector to
11 be more than the rest mass of a neutron. Also, the “other” energy deposited by background
12 events in the detector, will likely be concentrated in track or shower like structures. This is
13 in contrast to signal events, where the “other” energy depositions are likely to be isolated
14 depositions due to the spallation neutrons interacting in the detector. Classifying the structure
15 of the “other” energy depositions is not performed here, though it could be included should
16 any cosmic events appear to mimic a signal event. However, given the clear separation in the
17 amount of “other” energy deposited in the detector, it is not currently required.

18

19 Figure 6.21 shows the total energy attributed to both the kaon and to the electron, plus any
20 energy deposited near their shared interaction vertex, versus any “other” energy depositions.
21 Here, the total energy attributed to the kaon is plotted, including the energy deposited by the
22 kaon decay products, as was the case in Figure 6.20. As was seen in Figure 6.20, there is a
23 clear separation between the simulated signal events, and the cosmic background events. This
24 is again due to the large amount of “other” energy depositions observed in the background
25 sample. It is interesting to compare Figures 6.20b and 6.21b, as they are very similar. This
26 is to be expected from Figure 6.18b, where it was seen that the energy deposited by the
27 electron was rarely more than 10 MeV, and was never more than 100 MeV. This was in stark
28 contrast to Figure 6.18a, where the energy deposited in almost all of the electron showers
29 was more than 100 MeV. Hence, whilst there is a large difference in the energy plotted on the
30 y axis of Figures 6.20a and 6.21a, due to the addition of significant energy depositions from
31 the electron showers, there is relatively little difference the energy plotted on the y axis of
32 Figures 6.20b and 6.21b.

33

34 A significant difference between Figures 6.20a and 6.21a, is the relatively narrow band
35 of energies plotted on the y axis of Figure 6.21a, when compared to Figure 6.20a. This
36 is because of the relationship between the energy deposited by the kaon, the energy de-

posed by the electron shower, and the energy deposited near their shared interaction vertex.
 This was seen in Figure 6.19a, where the sum of the three energies was roughly 450 MeV.
 This means that for events where the kaon deposited relatively little energy, shown by the
 population of events at low total kaon energies in Figure 6.20a, the energy deposited by
 the electron shower, plus the energy deposited near the shared interaction vertex, will be large.

Following the application of all energy cuts, as outlined by the grey dashed boxes in
 Figures 6.18, 6.19, 6.20, and 6.21, only 24 of the 8,926 simulated signal events, which passed
 all subsequent cuts, are removed. If only the energy cuts, and the requirement that there be at
 least one kaon track, and at least one electron shower in the event, are applied, it is found that
 only 2 background candidates would survive the application of cuts. None of these events
 present serious contenders for signal events though, as they both fail the vertex and fiducial
 cuts, and have electrons which have very little energy (< 10 MeV).

Many of the signal events which are removed by the energy cuts have large amounts of
 “other” energy depositions, though they would no longer be removed if the limit on “other”
 depositions were raised to 200 MeV, as seen in Figure 6.21a. Though increasing the cut
 on “other” energy depositions to 200 MeV would still result in all background events being
 removed, it would mean that the limit was much closer to the regions of “other” energy
 depositions which are populated in Figures 6.20b, and 6.21b. As a result if a candidate
 event were to have between 100 and 200 MeV of energy depositions considered to be “other”
 energy depositions, its energy distributions would have to be carefully checked in order to
 verify that it is definitively not due to a background event. It is envisioned that the process
 by which this would be done, would be to consider how the “other” energy deposits are
 distributed in the detector, because, as discussed earlier, in a signal event it is likely that
 they would be isolated depositions, whereas in a background event, there would likely be
 “track-like” objects disconnected from the kaon and electron vertex.

Therefore, the result of a preliminary study on background rejection for the $n \rightarrow K^+ + e^-$
 decay channel, found no muon-induced background events which would survive the ap-
 plication of cuts, in a sample of 2×10^9 muons representing 401.6 years of detector for
 a single FD module. This corresponds to a limit of the background rate of less than 0.44
 events/Mt/year at the 90% confidence level, using double sided errors [25] and a fiducial
 mass of 13.8 kt to give an exposure of 5.542 Mt·year.

Using the cuts outlined above only 10.98% of signal events are removed, representing a high signal efficiency of 89.02%, where almost all of the signals which are removed due to at least one of the particles produced in the decay escaping the detector. When only particles which are fully contained in the active volume of the detector are considered the signal efficiency increases to 96.8%, where the 2 cm fiducial cut has removed most of the rejected signal events. These events have particles which travel close to the edge of the detector but do not quite leave it. For example, if the event shown in Figure 6.15 was a few cm further away from the edge of the detector, then this would be an example of an event which is fully contained in the detector but rejected by the fiducial cut. If it is apparent that a candidate event is contained in the detector, even though it deposits significant amounts of energy near the detector edge, it may be possible to still identify it as a neutron decay due to the lack of signal mimicking background events which were observed in this study. Therefore, it may be possible to increase the signal efficiencies quoted above by relaxing the 2 cm fiducial cut, though considering events where particles leave the active volume of the detector will mean that PID is more difficult, and the reconstructed energy may be much less than the rest mass of the neutron.

17

6.3.4 Future improvements to nucleon decay studies and conclusions

Thus far, the study of the background to nucleon decay has only focused on the muon-induced background. However, as was mentioned in Section 1.2.1 atmospheric neutrinos are also able to produce signal mimicking events in underground detectors. There have been no studies to date concerning the atmospheric background to the $n \rightarrow K^+ + e^-$ decay channel, though this will need to be performed before a full background estimation can be made for this decay channel. However, this is a separate study which will have to be performed at a later date.

25

The study of muon-induced background to nucleon decay presented in this thesis has only been performed on Monte Carlo truth information, and so has not used reconstructed objects. The extension of the analysis to include work on tracks is an important next step, as then the full analysis, which would be applied on real data, can be tested. Preliminary studies have begun on hit reconstruction, and involve running a filter on the muons used in the earlier analyses. This is because the number of events which are saved to disk would be prohibitive to running the full reconstruction process. As such, only events which meet the following criteria will be reconstructed [174]:

- 34 • A minimum of 10 MeV deposited in the detector volume.

- A maximum of 3,000 MeV deposited in the detector volume. 1
- A maximum of 5 MeV deposited within 10 cm of the detector edge. 2

These criteria are designed to be soft enough that the full range of nucleon decay modes can be studied, including di-nucleon decay modes and neutron-antineutron oscillations. This is why the maximum deposited energy greatly exceeds the rest mass of a single nucleon. This also accounts for the fact that during reconstruction some energy depositions may not be reconstructed, so even though the total energy deposited in the detector is 3 GeV, the total reconstructed energy may be less.

Upon performing reconstruction, and hence energy and position smearing, it is likely that the energy cuts which were outlined in Section 6.3.1 will have to be broadened. This may result in more background events being contained within the expected energy distributions for signal events, however the effectiveness of the cuts to remove background events should be largely unaffected. The reason for this, is that upon performing reconstruction, the separation of the kaon and electron track will not decrease, and so the cut is expected to remain very efficient. The only cut which may be less effective is the requirement that there only be one kaon track, and only one electron shower in the event. This is because some of the low energy electron showers may not be reconstructed. However, even when this cut was relaxed no background events survived the application of all cuts.

The reduced reconstruction efficiency will also affect the nucleon decay signals and so this, combined with the broader distributions of energies which will be reconstructed, will mean that the efficiency with which signal events can be identified will probably decrease. Studies have been performed to establish the event identification efficiencies when using reconstructed objects [175–178], though currently these have only been done with respect to the $p \rightarrow K^+ + \bar{\nu}_e$ decay channel. These studies have found that the current signal reconstruction efficiency is much less than the 100% assumed here, at around 30.5% [176], though it is imagined that this will improve significantly before the DUNE detector is built.

However, it is envisioned that there will still be no muon-induced background events which survive the application of all cuts, though the impact of atmospheric neutrinos remains to be seen, and so the observation of a single event in the DUNE detector could provide a robust indication of nucleon decay.

References

- [1] G. Aad et al. Observation of a new particle in the search for the Standard Model Higgs boson with the ATLAS detector at the LHC. *Phys. Lett.*, B716:1–29, 2012. 1
2
3
- [2] S. Chatrchyan et al. Observation of a new boson at a mass of 125 GeV with the CMS experiment at the LHC. *Phys. Lett.*, B716:30–61, 2012. 4
5
- [3] B. P. Abbott et al. Observation of gravitational waves from a binary black hole merger. *Phys. Rev. Lett.*, 116:061102, Feb 2016. 6
7
- [4] Y. Fukuda et al. Evidence for oscillation of atmospheric neutrinos. *Phys. Rev. Lett.*, 81:1562–1567, Aug 1998. 8
9
- [5] Q. R. Ahmad et al. Direct evidence for neutrino flavor transformation from neutral-current interactions in the sudbury neutrino observatory. *Phys. Rev. Lett.*, 89:011301, Jun 2002. 10
11
12
- [6] W. Pauli. Open letter to the Gauverein meeting in Tübingen, Dec 1930. 13
- [7] E. Fermi. An attempt of a theory of beta radiation. 1. *Z. Phys.*, 88:161–177, 1934. 14
- [8] O. Kofoed-Hansen. Maximum β -energies and the mass of the neutrino. *Phys. Rev.*, 71:451–452, Apr 1947. 15
16
- [9] G. C. Hanna and B. Pontecorvo. The β -spectrum of h^3 . *Phys. Rev.*, 75:983–984, Mar 1949. 17
18
- [10] L. M. Langer and R. J. D. Moffat. The beta-spectrum of tritium and the mass of the neutrino. *Phys. Rev.*, 88:689–694, Nov 1952. 19
20
- [11] C. L. Cowan, F. Reines, F. B. Harrison, H. W. Kruse, and A. D. McGuire. Detection of the free neutrino: A Confirmation. *Science*, 124:103–104, 1956. 21
22
- [12] G. Danby, J-M. Gaillard, K. Goulianos, L. M. Lederman, N. Mistry, M. Schwartz, and J. Steinberger. Observation of high-energy neutrino reactions and the existence of two kinds of neutrinos. *Phys. Rev. Lett.*, 9:36–44, Jul 1962. 23
24
25
- [13] R. Davis, D. S. Harmer, and K. C. Hoffman. Search for neutrinos from the sun. *Phys. Rev. Lett.*, 20:1205–1209, May 1968. 26
27
- [14] B. T. Cleveland et al. Measurement of the solar electron neutrino flux with the Homestake chlorine detector. *Astrophys. J.*, 496:505–526, 1998. 28
29

- ¹ [15] B. Pontecorvo. Mesonium and anti-mesonium. *Sov. Phys. JETP*, 6:429, 1957. [*Zh. Eksp. Teor. Fiz.*33,549(1957)].
- ³ [16] K. S. Hirata et al. Observation of ${}^8\text{B}$ solar neutrinos in the kamiokande-ii detector. *Phys. Rev. Lett.*, 63:16–19, Jul 1989.
- ⁵ [17] M. L. Perl et al. Evidence for anomalous lepton production in $e^+ - e^-$ annihilation. *Phys. Rev. Lett.*, 35:1489–1492, Dec 1975.
- ⁷ [18] K. Kodama et al. Observation of tau neutrino interactions. *Physics Letters B*, 504(3):218 – 224, 2001.
- ⁹ [19] Q. R. Ahmad et al. Measurement of the rate of $\nu_e + d \rightarrow p + p + e^-$ interactions produced by ${}^8\text{B}$ solar neutrinos at the Sudbury Neutrino Observatory. *Phys. Rev. Lett.*, 87:071301, 2001.
- ¹² [20] Z. Maki, M. Nakagawa, and S. Sakata. Remarks on the unified model of elementary particles. *Progress of Theoretical Physics*, 28(5):870, 1962.
- ¹⁴ [21] S. Andringa et al. Current Status and Future Prospects of the SNO+ Experiment. *Adv. High Energy Phys.*, 2016:6194250, 2016.
- ¹⁶ [22] R. Arnold et al. Probing new physics models of neutrinoless double beta decay with supernemo. *The European Physical Journal C*, 70(4):927–943, 2010.
- ¹⁸ [23] G. Tzanankos et al. MINOS+: a Proposal to FNAL to run MINOS with the medium energy NuMI beam. 2011.
- ²⁰ [24] H. Nunokawa, S. J. Parke, and J. W. F. Valle. CP Violation and Neutrino Oscillations. *Prog. Part. Nucl. Phys.*, 60:338–402, 2008.
- ²² [25] C. Patrignani et al. Review of Particle Physics. *Chin. Phys.*, C40(10):100001, 2016.
- ²³ [26] Nicola Cabibbo. Unitary symmetry and leptonic decays. *Phys. Rev. Lett.*, 10:531–533, Jun 1963.
- ²⁵ [27] Makoto Kobayashi and Toshihide Maskawa. CP Violation in the Renormalizable Theory of Weak Interaction. *Prog. Theor. Phys.*, 49:652–657, 1973.
- ²⁷ [28] L. Wolfenstein. Neutrino oscillations in matter. *Phys. Rev. D*, 17:2369–2374, May 1978.
- ²⁹ [29] S. P. Mikheev and A. Yu. Smirnov. Resonance Amplification of Oscillations in Matter and Spectroscopy of Solar Neutrinos. *Sov. J. Nucl. Phys.*, 42:913–917, 1985. [*Yad. Fiz.*42,1441(1985)].
- ³² [30] *Fundamental Physics at the Intensity Frontier*, 2012.
- ³³ [31] I. Esteban et al. Updated fit to three neutrino mixing: exploring the accelerator-reactor complementarity. *JHEP*, 01:087, 2017.
- ³⁵ [32] P. A. R. Ade et al. Planck 2015 results. XIII. Cosmological parameters. *Astron. Astrophys.*, 594:A13, 2016.

-
- [33] Susanne Mertens. Status of the katrin experiment and prospects to search for kev-mass sterile neutrinos in tritium β -decay. *Physics Procedia*, 61:267 – 273, 2015. 1
2
- [34] S. Schael et al. Precision electroweak measurements on the Z resonance. *Phys. Rept.*, 427:257–454, 2006. 3
4
- [35] C. Athanassopoulos et al. Results on $\nu_\mu \rightarrow \nu_e$ neutrino oscillations from the lsnd experiment. *Phys. Rev. Lett.*, 81:1774–1777, Aug 1998. 5
6
- [36] A. Aguilar et al. Evidence for neutrino oscillations from the observation of $\bar{\nu}_e$ appearance in a $\bar{\nu}_\mu$ beam. *Phys. Rev. D*, 64:112007, Nov 2001. 7
8
- [37] A. A. Aguilar-Arevalo et al. Improved search for $\bar{\nu}_\mu \rightarrow \bar{\nu}_e$ oscillations in the mini-boone experiment. *Phys. Rev. Lett.*, 110:161801, Apr 2013. 9
10
- [38] Goran Senjanovic. Proton decay and grand unification. *AIP Conf. Proc.*, 1200:131–141, 2010. 11
12
- [39] Howard Georgi and S. L. Glashow. Unity of all elementary-particle forces. *Phys. Rev. Lett.*, 32:438–441, Feb 1974. 13
14
- [40] Hermann Weyl. Elektron und gravitation. i. *Zeitschrift für Physik*, 56(5):330–352, 1929. 15
16
- [41] Francesco Vissani. (B+L) conserving nucleon decays in supersymmetric models. *Phys. Rev.*, D52:4245–4247, 1995. 17
18
- [42] G. Battistoni et al. Nucleon stability, magnetic monopoles and atmospheric neutrinos in the mont-blanc experiment. *Physics Letters B*, 133(6):454 – 460, 1983. 19
20
- [43] C. Berger et al. Lifetime limits on ($B - L$)-violating nucleon decay and di-nucleon decay modes from the Frejus experiment. *Physics Letters B*, 269:227–233, 1991. 21
22
- [44] M. C Goodman. Nucleon Decay in Soudan-2. In *Proceedings of the 26th International Cosmic Ray Conference. August 17-25, 1999. Salt Lake City, Utah, USA*, page 364, 1999. 23
24
25
- [45] W. Gajewski et al. Search for proton decay into e+ + pi0 in IMB-3 detector. *Phys. Rev.*, D42:2974–2976, 1990. 26
27
- [46] K. Abe et al. Search for proton decay via $p \rightarrow e^+ \pi^0$ and $p \rightarrow \mu^+ \pi^0$ in 0.31 megaton · years exposure of the super-kamiokande water cherenkov detector. *Phys. Rev. D*, 95:012004, Jan 2017. 28
29
30
- [47] K. Abe et al. Letter of Intent: The Hyper-Kamiokande Experiment — Detector Design and Physics Potential —. 2011. 31
32
- [48] Dorota Stefan and Artur M. Ankowski. Nuclear effects in proton decay. *Acta Phys. Polon.*, B40:671–674, 2009. 33
34
- [49] S. Ritz et al. Building for Discovery: Strategic Plan for U.S. Particle Physics in the Global Context. 2014. 35
36

References

232

- 1 [50] LBNE Collaboration. Long-Baseline Neutrino Experiment (LBNE) Project, Volume
2 1: The LBNE Project. Technical Report LBNE-doc-5235, Oct 2012.
- 3 [51] LBNE Collaboration. Long-Baseline Neutrino Experiment (LBNE) Project, Volume
4 2: The Beamline at the Near Site. Technical Report LBNE-doc-4317, Oct 2012.
- 5 [52] LBNE Collaboration. Long-Baseline Neutrino Experiment (LBNE) Project, Volume
6 3: Detectors at the Near Site. Technical Report LBNE-doc-4724, Oct 2012.
- 7 [53] LBNE Collaboration. Long-Baseline Neutrino Experiment (LBNE) Project, Volume
8 4: The Liquid Argon Detector at the Far Site. Technical Report LBNE-doc-4892, Oct
9 2012.
- 10 [54] LBNE Collaboration. Long-Baseline Neutrino Experiment (LBNE) Project, Volume
11 5: Conventional Facilities at the Near Site. Technical Report LBNE-doc-4623, Oct
12 2012.
- 13 [55] LBNE Collaboration. Long-Baseline Neutrino Experiment (LBNE) Project, Volume 6:
14 Conventional Facilities at the Far Site. Technical Report LBNE-doc-5017, Oct 2012.
- 15 [56] A. Stahl et al. Expression of Interest for a very long baseline neutrino oscillation
16 experiment (LBNO). 2012.
- 17 [57] R. Acciarri et al. Long-Baseline Neutrino Facility (LBNF) and Deep Underground
18 Neutrino Experiment (DUNE), Volume 1: The LBNF and DUNE Projects. 2016.
- 19 [58] R. Acciarri et al. Long-Baseline Neutrino Facility (LBNF) and Deep Underground
20 Neutrino Experiment (DUNE), Volume 2: The Physics Program for DUNE at LBNF.
21 2015.
- 22 [59] J. Strait et al. Long-Baseline Neutrino Facility (LBNF) and Deep Underground
23 Neutrino Experiment (DUNE), Volume 3: Long-Baseline Neutrino Facility for DUNE.
24 2016.
- 25 [60] R. Acciarri et al. Long-Baseline Neutrino Facility (LBNF) and Deep Underground
26 Neutrino Experiment (DUNE), Volume 4: The DUNE Detectors at LBNF. 2016.
- 27 [61] DUNE Collaboration. Proposals and Design Reports. [online] <https://web.fnal.gov/project/LBNF/SitePages/Proposals%20and%20Design%20Reports.aspx>.
- 28 [62] S.D. Holmes et al. PIP-II Status and Strategy. *Proc. of IPAC2015*, pages 3982–3985,
29 2015.
- 30 [63] Y.K. Kim et al. LBNE Reconfiguration: Steering Committee Report, Aug 2012.
31 [online] <https://indico.fnal.gov/getFile.py/access?contribId=2&resId=0&materialId=slides&confId=11627>.
- 32 [64] [online] <http://www.sanfordlab.org>.
- 33 [65] A. Rubbia. Final Report Summary - LAGUNA-LBNO (Design of a pan-European
34 Infrastructure for Large Apparatus studying Grand Unification, Neutrino Astrophysics
35 and Long Baseline Neutrino Oscillations), Dec 2015.

-
- [66] A. Badertscher et al. First operation and performance of a 200 lt double phase lar lem-tpc with a 40×76 cm² readout. *Journal of Instrumentation*, 8(04):P04012, 2013. 1
2
- [67] A. Badertscher et al. First operation and drift field performance of a large area double phase lar electron multiplier time projection chamber with an immersed greinacher high-voltage multiplier. *Journal of Instrumentation*, 7(08):P08026, 2012. 3
4
5
- [68] A. Badertscher et al. First operation of a double phase LAr Large Electron Multiplier Time Projection Chamber with a two-dimensional projective readout anode. *Nucl. Instrum. Meth.*, A641:48–57, 2011. 6
7
8
- [69] J. E. Campagne et al. Pmm²: R&d on triggerless acquisition for next generation neutrino experiments. *Journal of Instrumentation*, 6(01):C01081, 2011. 9
10
- [70] B. Genolini et al. PMm²: Large photomultipliers and innovative electronics for the next-generation neutrino experiments. *Nucl. Instrum. Meth.*, A610:249–252, 2009. 11
12
- [71] E. Worcester. PRESENTING LONG-BASELINE SENSITIVITIES. Technical Report DUNE-doc-2329, Jan 2017. 13
14
- [72] M. Bass et al. Baseline Optimization for the Measurement of CP Violation, Mass Hierarchy, and θ_{23} Octant in a Long-Baseline Neutrino Oscillation Experiment. *Phys. Rev.*, D91(5):052015, 2015. 15
16
17
- [73] Milind V. Diwan. The Case for a super neutrino beam. *Frascati Phys. Ser.*, 35:89–109, 2004. [,89(2004)]. 18
19
- [74] E. Worcester. LBL CPV Sensitivity: Standard Exposures. Technical Report DUNE-doc-2332, Feb 2017. 20
21
- [75] E. Worcester. LBL MH Sensitivity: Standard Exposures. Technical Report DUNE-doc-2335, Feb 2017. 22
23
- [76] E. Worcester. LBL Sensitivity: Staging Plots. Technical Report DUNE-doc-2377, Feb 2017. 24
25
- [77] E. Worcester. LBL CPV Sensitivity: Exposure Plots. Technical Report DUNE-doc-2401, Feb 2017. 26
27
- [78] E. Worcester. LBL MH Sensitivity: Exposure Plots. Technical Report DUNE-doc-2407, Feb 2017. 28
29
- [79] J. Beringer et al. Review of particle physics. *Phys. Rev. D*, 86:010001, Jul 2012. 30
- [80] H. Nishino et al. Search for Nucleon Decay into Charged Anti-lepton plus Meson in Super-Kamiokande I and II. *Phys. Rev.*, D85:112001, 2012. 31
32
- [81] A. Bueno, Z. Dai, Y. Ge, M. Laffranchi, A. J. Melgarejo, A. Meregaglia, Sergio Navas, and A. Rubbia. Nucleon decay searches with large liquid argon TPC detectors at shallow depths: Atmospheric neutrinos and cosmogenic backgrounds. *JHEP*, 04:041, 2007. 33
34
35
36

- ¹ [82] J. Klinger, V. A. Kudryavtsev, M. Richardson, and N. J. C. Spooner. Muon-induced
² background to proton decay in the $p \rightarrow K^+ \nu$ decay channel with large underground
³ liquid argon TPC detectors. *Phys. Lett.*, B746:44–47, 2015.
- ⁴ [83] M. Antonello et al. Precise 3D track reconstruction algorithm for the ICARUS T600
⁵ liquid argon time projection chamber detector. *Adv. High Energy Phys.*, 2013:260820,
⁶ 2013.
- ⁷ [84] L. Lin and M. Goodman. Comprehensive list of nucleon decay modes. Technical
⁸ Report DUNE-doc-679, Apr 2016.
- ⁹ [85] C. Adams et al. The Long-Baseline Neutrino Experiment: Exploring Fundamental
¹⁰ Symmetries of the Universe. 2013.
- ¹¹ [86] A. Blake. Studying Atmospheric Neutrino Backgrounds to $p \rightarrow K^+ \bar{\nu} e$ Decay. Technical
¹² Report LBNE-doc-8836, Apr 2014.
- ¹³ [87] K. Scholberg. Supernova neutrino detection. *Annual Review of Nuclear and Particle
Science*, 62(1):81–103, 2012.
- ¹⁵ [88] R. Laha and J. F. Beacom. Gadolinium in water Cherenkov detectors improves
¹⁶ detection of supernova ν_e . *Phys. Rev.*, D89:063007, 2014.
- ¹⁷ [89] R. M. Bionta et al. Observation of a neutrino burst in coincidence with supernova
¹⁸ 1987a in the large magellanic cloud. *Phys. Rev. Lett.*, 58:1494–1496, Apr 1987.
- ¹⁹ [90] K. Hirata et al. Observation of a neutrino burst from the supernova sn1987a. *Phys.
Rev. Lett.*, 58:1490–1493, Apr 1987.
- ²¹ [91] L. Hudepohl, B. Muller, H. T. Janka, A. Marek, and G. G. Raffelt. Neutrino Signal
²² of Electron-Capture Supernovae from Core Collapse to Cooling. *Phys. Rev. Lett.*,
²³ 104:251101, 2010. [Erratum: *Phys. Rev. Lett.* 105, 249901(2010)].
- ²⁴ [92] M. G. Aartsen et al. Search for dark matter annihilations in the Sun with the 79-string
²⁵ IceCube detector. *Phys. Rev. Lett.*, 110(13):131302, 2013.
- ²⁶ [93] K. Choi et al. Search for neutrinos from annihilation of captured low-mass dark matter
²⁷ particles in the Sun by Super-Kamiokande. *Phys. Rev. Lett.*, 114(14):141301, 2015.
- ²⁸ [94] J. F. Beacom. The Diffuse Supernova Neutrino Background. *Ann. Rev. Nucl. Part.
Sci.*, 60:439–462, 2010.
- ³⁰ [95] O. L. Caballero, G. C. McLaughlin, and R. Surman. Neutrino Spectra from Accretion
³¹ Disks: Neutrino General Relativistic Effects and the Consequences for Nucleosynthesis.
³² *Astrophys. J.*, 745:170, 2012.
- ³³ [96] O. L. Caballero, G. C. McLaughlin, R. Surman, and R. Surman. Detecting neutrinos
³⁴ from black hole neutron stars mergers. *Phys. Rev.*, D80:123004, 2009.
- ³⁵ [97] M. Thomson. DUNE Collaboration, Strategy and Detector Requirements. Technical
³⁶ Report LBNE-doc-11100, June 2015.

-
- [98] M. Adamowski et al. The Liquid Argon Purity Demonstrator. *JINST*, 9:P07005, 2014. 1
- [99] D. Montanari et al. Performance and Results of the LBNE 35 Ton Membrane Cryostat Prototype. *Phys. Procedia*, 67:308–313, 2015. 2
3
- [100] A. Hahn et al. The LBNE 35 Ton Prototype Cryostat. In *Proceedings, 21st Symposium on Room-Temperature Semiconductor X-ray and Gamma-ray Detectors (RTSD 2014): Seattle, WA, USA, November 8-15, 2014*, page 7431158, 2016. 4
5
6
- [101] E. D. Church. LArSoft: A Software Package for Liquid Argon Time Projection Drift Chambers. 2013. 7
8
- [102] The LArSoft collabortion. Software for LArTPCs, 2017. [online] <http://larsoft.org>. 9
- [103] R. Brun and F. Rademakers. ROOT: An object oriented data analysis framework. *Nucl. Instrum. Meth.*, A389:81–86, 1997. 10
11
- [104] S. Agostinelli et al. Geant4—a simulation toolkit. *Nuclear Instruments and Methods in Physics Research Section A: Accelerators, Spectrometers, Detectors and Associated Equipment*, 506(3):250 – 303, 2003. 12
13
14
- [105] C. Andreopoulos et al. The GENIE neutrino Monte Carlo generator. *Nuclear Instruments and Methods in Physics Research Section A: Accelerators, Spectrometers, Detectors and Associated Equipment*, 614(1):87 – 104, 2010. 15
16
17
- [106] D. Casper. The Nuance neutrino physics simulation, and the future. *Nucl. Phys. Proc. Suppl.*, 112:161–170, 2002. [,161(2002)]. 18
19
- [107] C. Hagman et al. Cosmic-ray Shower Library CRY, 2012. [online] http://nuclear.llnl.gov/simulation/doc_cry_v1.7/cry.pdf. 20
21
- [108] C. Hagmann, D. Lange, and D. Wright. Monte carlo simulation of proton-induced cosmic-ray cascades in the atmosphere. *Lawrence Livermore National Laboratory*, 2007. 22
23
24
- [109] D. Heck, G. Schatz, J. Knapp, T. Thouw, and J.N. Capdevielle. CORSIKA: A Monte Carlo code to simulate extensive air showers. Technical report, 1998. 25
26
- [110] V.A. Kudryavtsev. Muon simulation codes MUSIC and MUSUN for underground physics. *Computer Physics Communications*, 180(3):339 – 346, 2009. 27
28
- [111] V. A. Kudryavtsev, N. J. C. Spooner, and J. E. McMillan. Simulations of muon induced neutron flux at large depths underground. *Nucl. Instrum. Meth.*, A505:688–698, 2003. 29
30
- [112] P. Antonioli, C. Ghetti, E. V. Korolkova, V. A. Kudryavtsev, and G. Sartorelli. A Three-dimensional code for muon propagation through the rock: Music. *Astropart. Phys.*, 7:357–368, 1997. 31
32
33
- [113] V. A. Kudryavtsev, E. V. Korolkova, and N. J. C. Spooner. Narrow muon bundles from muon pair production in rock. *Phys. Lett.*, B471:251–256, 1999. 34
35
- [114] T. Alion. LBNE Geometries, Aug 2014. [online] https://cdcvn.fnal.gov/redmine/projects/lbnecode/wiki/LBNE_Geometries. 36
37

- ¹ [115] J. Asaadi et al. The Current Status of Simulation and Reconstruction for the DUNE Far Detector. Technical Report DUNE-doc-1689, Sept 2016.
- ³ [116] C. Harris and M. Stephens. A combined corner and edge detector. Citeseer, 1988.
- ⁴ [117] P. V. C. Hough. Machine Analysis Of Bubble Chamber Pictures. In *Proceedings, 2nd International Conference on High-Energy Accelerators and Instrumentation, HEACC 1959: CERN, Geneva, Switzerland, September 14-19, 1959*, volume C590914, pages 554–558, 1959.
- ⁸ [118] J. S. Marshall and M. A. Thomson. The Pandora Software Development Kit for Pattern Recognition. *Eur. Phys. J.*, C75(9):439, 2015.
- ¹⁰ [119] M. Wallbank. EMShower Reconstruction. Technical Report DUNE-doc-1369, June 2016.
- ¹² [120] J. B. Birks. The efficiency of organic scintillatois. *ORGANIC*, page 12, 1960.
- ¹³ [121] R. Acciarri et al. A study of electron recombination using highly ionizing particles in the ArgoNeuT Liquid Argon TPC. *JINST*, 8:P08005, 2013.
- ¹⁵ [122] J. Thomas and D. A. Imel. Recombination of electron-ion pairs in liquid argon and liquid xenon. *Phys. Rev. A*, 36:614–616, Jul 1987.
- ¹⁷ [123] A. Blatter et al. Experimental study of electric breakdowns in liquid argon at centimeter scale. *Journal of Instrumentation*, 9(04):P04006, 2014.
- ¹⁹ [124] S. C. Delaquis, R. Gornea, S. Janos, M. Lüthi, C. Rudolf von Rohr, M. Schenk, and J. L. Vuilleumier. Development of a camera casing suited for cryogenic and vacuum applications. *JINST*, 8:T12001, 2013.
- ²² [125] K. Mavrokordidis, F. Ball, J. Carroll, M. Lazos, K. J. McCormick, N. A. Smith, C. Touramanis, and J. Walker. Optical Readout of a Two Phase Liquid Argon TPC using CCD Camera and THGEMs. *JINST*, 9:P02006, 2014.
- ²⁵ [126] E. Erdal, L. Arazi, V. Chepe, M. L. Rappaport, D. Vartsky, and A. Breskin. Direct observation of bubble-assisted electroluminescence in liquid xeno. *JINST*, 10(11):P11002, 2015.
- ²⁸ [127] N. McConkey, N. Spooner, M. Thiesse, M. Wallbank, and T. K. Warburton. Cryogenic CMOS Cameras for High Voltage Monitoring in Liquid Argon. 2016.
- ³⁰ [128] G. Ghibaudo and F. Balestra. Low temperature characterization of silicon cmos devices. *Microelectronics Reliability*, 37(9):1353 – 1366, 1997.
- ³² [129] H. Zhao and X. Liu. A low-power cryogenic analog to digital converter in standard CMOS technology. *Cryogenics*, 55:79–83, May 2013.
- ³⁴ [130] M. Antonello et al. A Proposal for a Three Detector Short-Baseline Neutrino Oscillation Program in the Fermilab Booster Neutrino Beam. 2015.
- ³⁶ [131] H. Bethe. Zur theorie des durchgangs schneller korpuskularstrahlen durch materie. *Annalen der Physik*, 397(3):325–400, 1930.

-
- [132] F. Bloch. Zur bremsung rasch bewegter teilchen beim durchgang durch materie. *Annalen der Physik*, 408(3):285–320, 1933. 1
2
- [133] X. Qian. A Four-Plane proposal for Single-Phase LArTPC. Far Detector Sim/Reco working group meeting, Sept 2016. [online] <https://indico.fnal.gov/getFile.py/access?contribId=78&sessionId=20&resId=0&materialId=slides&confId=10613>. 3
4
5
- [134] J. Insler. Module to unstick ADC codes. 35 ton working group meeting, Mar 2016. [online] <https://indico.fnal.gov/getFile.py/access?contribId=2&resId=0&materialId=slides&confId=11627>. 6
7
8
- [135] MicroBooNE Collaboration. Noise Characterization and Filtering in the MicroBooNE TPC. Technical Report MICROBOONE-NOTE-1016-PUB, July 2016. 9
10
- [136] J. Cooley and J. Turkey. An algorithm for the machine calculation of complex fourier series. *Math. Comp.*, 19:297–301, 1965. 11
12
- [137] N. Wiener. *Extrapolation, Interpolation, and Smoothing of Stationary Time Series*. [Cambridge]: Technology Press of the Massachusetts Institute of Technology., 1942. 13
14
- [138] M. Johnson et al. 35T Observations and Measurements. Technical Report DUNE-doc-1704, Aug 2016. 15
16
- [139] L. Bagby et al. 35T Noise Studies Summary - APA wire readout noise. Technical Report DUNE-doc-1834, Oct 2016. 17
18
- [140] T. Yang. Update on reconstruction of 35t data. 35 ton working group meeting, June 2016. [online] <https://indico.fnal.gov/getFile.py/access?contribId=1&resId=0&materialId=slides&confId=12349>. 19
20
21
- [141] P.H.S Torr and A. Zisserman. Mlesac: A new robust estimator with application to estimating image geometry. *Computer Vision and Image Understanding*, 78(1):138–156, 2000. 22
23
24
- [142] M. Thiesse. Hit reconstruction and purity. 35 ton working group meeting, Aug 2016. [online] <https://indico.fnal.gov/getFile.py/access?contribId=1&resId=0&materialId=slides&confId=12859>. 25
26
27
- [143] C. Anderson et al. The ArgoNeuT Detector in the NuMI Low-Energy beam line at Fermilab. *JINST*, 7:P10019, 2012. 28
29
- [144] T. Yang. Update on 35 ton analysis. 35 ton working group meeting, June 2016. [online] <https://indico.fnal.gov/getFile.py/access?contribId=1&resId=0&materialId=slides&confId=12396>. 30
31
32
- [145] S.E. Derenzo et al. Test of a liquid argon chamber with 20 μm RMS resolution. *Nuclear Instruments and Methods*, 122:319–327, December 1974. 33
34
- [146] S. E. Derenzo. LBL Physics Note No. 786: Electron diffusion and positive ion charge retention in liquid-filled high-resolution multi- strip ionization-mode chambers. unpublished, 1974. 35
36
37

- ¹ [147] E. Shibamura, T. Takahashi, S. Kubota, and T. Doke. Ratio of diffusion coefficient to
² mobility for electrons in liquid argon. *Phys. Rev. A*, 20:2547–2554, Dec 1979.
- ³ [148] V. M. Atrazhev and I. V. Timoshkin. Trasport of electrons in atomic liquids in high
⁴ electric fields. *IEEE Trans. Dielectrics and Electrical Insulation*, 5:450–457, 1998.
- ⁵ [149] Y. Li et al. Measurement of Longitudinal Electron Diffusion in Liquid Argon. *Nucl.
6 Instrum. Meth.*, A816:160–170, 2016.
- ⁷ [150] D. Brailsford. Looking at electron diffusion in 35t data and MC. 35 ton working group
⁸ meeting, Sept 2016. [online] [https://indico.fnal.gov/getFile.py/access?contribId=43&
9 sessionID=19&resId=0&materialId=slides&confId=10613](https://indico.fnal.gov/getFile.py/access?contribId=43&sessionID=19&resId=0&materialId=slides&confId=10613).
- ¹⁰ [151] C Bromberg et al. Design and operation of longbo: a 2 m long drift liquid argon tpc.
¹¹ *Journal of Instrumentation*, 10(07):P07015, 2015.
- ¹² [152] M. Richardson. *Cosmic ray background estimations in large liquid argon detectors
13 for proton decay via $p \rightarrow K^+ \bar{v}$ and ν_e appearance from ν_μ beam*. PhD thesis, The
¹⁴ University of Sheffield, 2016.
- ¹⁵ [153] N. S. Bowden. Review Report: Mini-Review of Operation of the LBNE Far Detector
¹⁶ at the Surface. Technical Report LBNE-doc-6493, Oct 2012.
- ¹⁷ [154] D. Wright. Shielding Physics List Description, June 2012. [online] [http://www.slac.
18 stanford.edu/comp/physics/geant4/slac_physics_lists/shielding/physlistdoc.html](http://www.slac.stanford.edu/comp/physics/geant4/slac_physics_lists/shielding/physlistdoc.html).
- ¹⁹ [155] B. Baller. LAr-FD Parameters Spreadsheet. Technical Report LBNE-doc-3383, Aug
²⁰ 2015.
- ²¹ [156] D. Cherdack. The LBNE Fast MC. Technical Report LBNE-doc-7806, Sept 2013.
- ²² [157] D. Barker et al. Muon-induced background for beam neutrinos at
²³ the surface. LBNE Reconfiguration Report, Aug 2012. [online]
²⁴ [http://www.fnal.gov/directorate/lbne_reconfiguration/files/LBNE-Reconfiguration-
25 Surface-Detector-August2012.pdf](http://www.fnal.gov/directorate/lbne_reconfiguration/files/LBNE-Reconfiguration-Surface-Detector-August2012.pdf).
- ²⁶ [158] D. Mei, C. Zhang, and D. Barker. USD Cosmogenics Backgrounds Simulation
²⁷ Overview. Technical Report LBNE-doc-6621, Nov 2012.
- ²⁸ [159] D. Coelho, M. Szydagis, and R. Svoboda. Improving Electron / Gamma Separation.
²⁹ Technical Report LBNE-doc-8458, Nov 2012.
- ³⁰ [160] A. Hitachi et al. Effect of ionization density on the time dependence of luminescence
³¹ from liquid argon and xenon. *Phys. Rev. B*, 27:5279–5285, May 1983.
- ³² [161] T. K. Gaisser. *Cosmic rays and particle physics*. Cambridge, UK: Univ. Pr. (1990)
³³ 279 p, 1990.
- ³⁴ [162] M. Aglietta et al. Muon “depth-intensity” relation measured by the lvd underground
³⁵ experiment and cosmic-ray muon spectrum at sea level. *Phys. Rev. D*, 58:092005, Oct
³⁶ 1998.

-
- [163] A. Dar. Atmospheric neutrinos, astrophysical neutrons, and proton-decay experiments. *Phys. Rev. Lett.*, 51:227–230, Jul 1983. 1
2
- [164] T. Blackwell, V. A. Kudryavtsev, and M. Richardson. Cosmic-ray Spectra from CRY. Technical Report LBNE-doc-7517, July 2013. 3
4
- [165] G. J. Feldman and R. D. Cousins. Unified approach to the classical statistical analysis of small signals. *Phys. Rev. D*, 57:3873–3889, Apr 1998. 5
6
- [166] D. M. Mei, C. Zhang, K. Thomas, and F. Gray. Early Results on Radioactive Background Characterization for Sanford Laboratory and DUSEL Experiments. *Astropart. Phys.*, 34:33–39, 2010. 7
8
9
- [167] F. E. Gray et al. Cosmic Ray Muon Flux at the Sanford Underground Laboratory at Homestake. *Nucl. Instrum. Meth.*, A638:63–66, 2011. 10
11
- [168] J. Heise. The Sanford Underground Research Facility at Homestake. *AIP Conf. Proc.*, 1604:331–344, 2014. 12
13
- [169] M. L. Cherry, M. Deakyne, K. Lande, C. K. Lee, R. I. Steinberg, B. Cleveland, and E. J. Fenyves. Multiple muons in the homestake underground detector. *Phys. Rev. D*, 27:1444–1447, Apr 1983. 14
15
16
- [170] N. Abgrall et al. Muon Flux Measurements at the Davis Campus of the Sanford Underground Research Facility with the Majorana Demonstrator Veto System. 2016. 17
18
- [171] E. Church. September 2016 Progress Report from the Atmospheric Neutrinos, Nucleon Decay, and Cosmogenics Working Groups. Technical Report DUNE-doc-1644, Sept 2016. 19
20
21
- [172] de Jong. J. K. Atmospheric Muon Simulation for LBNE. Technical Report LBNE-doc-3144, July 2012. 22
23
- [173] V. A. Kudryavtsev et al. Muon simulations for LBNE using MUSIC and MUSUN. Technical Report LBNE-doc-9673, Sept 2014. 24
25
- [174] M. Robinson. Cosmogenic background to nucelon decay. Cosmogenics working group meeting, Jan 2017. [online] <https://indico.fnal.gov/getFile.py/access?contribId=104&sessionId=14&resId=0&materialId=slides&confId=10641>. 26
27
28
- [175] K. Wood. Reconstruction efficiencies of scintillation light from pdk events. Cosmogenics working group meeting, Sept 2016. [online] <https://indico.fnal.gov/getFile.py/access?contribId=98&sessionId=25&resId=0&materialId=slides&confId=10613>. 29
30
31
- [176] A. Higuera. Proton decay at dune $p \rightarrow k^+ + \bar{\nu}_e$. Cosmogenics working group meeting, Feb 2017. [online] <https://indico.fnal.gov/getFile.py/access?contribId=1&resId=0&materialId=slides&confId=13789>. 32
33
34
- [177] T. Yang. Updates on reconstruction. Cosmogenics working group meeting, Feb 2017. [online] <https://indico.fnal.gov/getFile.py/access?contribId=2&resId=0&materialId=slides&confId=13789>. 35
36
37

-
- ¹ [178] A. Higuera. Proton decay at dune $p \rightarrow k^+ + \overline{\nu}_e$ and ${}^{39}\text{ar}$. Cosmogenics working group
² meeting, Mar 2017. [online] [https://indico.fnal.gov/getFile.py/access?contribId=3&](https://indico.fnal.gov/getFile.py/access?contribId=3&resId=0&materialId=slides&confId=13947)
³